Uncovering network mechanism underlying thalamic Deep Brain Stimulation using a novel firing rate model

Yupeng Tian, Edward Bello, David Crompton, Suneil K. Kalia, Mojgan Hodaie, Andres M. Lozano, William D. Hutchison, Matthew D. Johnson, Milos R. Popovic, Luka Milosevic, Milad Lankarany

Graphical abstract

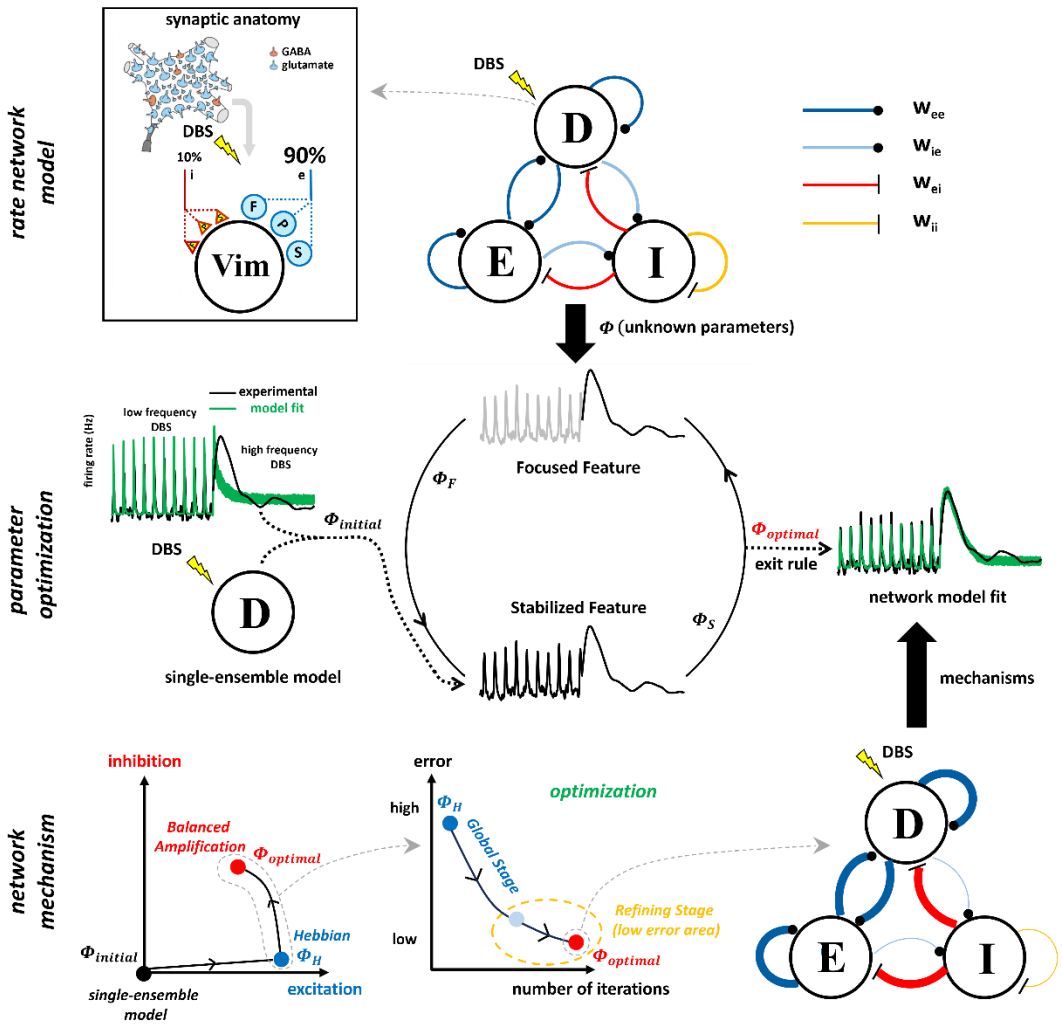

Uncovering network mechanism underlying thalamic Deep Brain Stimulation using a novel firing rate model

Yupeng Tian [1,2,4,5], Edward Bello [6], David Crompton [1,2,4,5], Suneil K. Kalia [1,4,5,7,8], Mojgan Hodaie [1,5,7,8], Andres M. Lozano [1,5,7,8], William D. Hutchison [3,5,7], Matthew D. Johnson [6], Milos R. Popovic [2,4,5], Luka Milosevic [1,2,4,5], Milad Lankarany [1,2,3,4,5]*

[1] Krembil Research Institute – University Health Network, Toronto, ON, Canada

[2] Institute of Biomedical Engineering, University of Toronto, Toronto, ON, Canada

[3] Department of Physiology, University of Toronto, Toronto, ON, Canada

[4] KITE Research Institute, Toronto Rehabilitation Institute - University Health Network, Toronto, ON, Canada

[5] CRANIA, University Health Network and University of Toronto, Toronto, Canada.

[6] Department of Biomedical Engineering, University of Minnesota

[7] Department of Surgery, University of Toronto, Toronto, Canada

[8] Division of Neurosurgery, Toronto Western Hospital, University Health Network, Toronto, Canada

* To whom correspondence should be addressed:
Milad Lankarany, Email: milad.lankarany@uhn.ca
The Krembil Research Institute – University Health Network (UHN)
60 Leonard Ave, Toronto, M5T 0S8, Canada

ABSTRACT

Thalamic ventral intermediate nucleus (Vim) is the primary surgical target of deep brain stimulation (DBS) for reducing symptoms of essential tremor. In-vivo single unit recordings of patients with essential tremor revealed that low frequency Vim-DBS (≤50Hz) induces periodic excitatory responses and high-frequency Vim-DBS (≥100Hz) induces a transient excitatory response lasting for ⩽600ms followed by a suppressed steady-state. Yet, the neural mechanisms that generate Vim firing rate in response to different DBS frequencies are not fully uncovered. Previously developed models of Vim neurons could not capture the full dynamics of Vim-DBS despite incorporating the dynamics of short-term synaptic plasticity. In this work, we developed a network rate model and a novel parameter optimization method to accurately track the instantaneous firing rate of Vim neurons in response to various DBS frequencies, ranging in low- and high-frequency (5 to 200Hz) Vim-DBS. We showed that the firing rate dynamics during high frequency Vim-DBS are best characterized when incorporating an inhibitory population into the network model. Further, we discovered that the Vim firing rate in response to varying frequencies of DBS pulses can be explained by a *balanced amplification* mechanism, in which strong excitation (Vim) is stabilized by equally strong feedback inhibition. As a further validation of this work, we demonstrated similar behavior in a detailed biophysical model consisting of spiking neural networks in which the Vim neural-network can implement balanced amplification and explain in-vivo human Vim-DBS observations.

INTRODUCTION

Deep brain stimulation (DBS) delivers electrical pulses to adjacent neural circuits and is known to modulate neural activity [1,2,3]. DBS has become a standard therapy for many movement disorders, including Parkinson's disease [2], essential tremor [3], and dystonia [4]. DBS is now being investigated as a treatment for psychiatric and cognitive disorders, including obsessive-compulsive disorder [5] and Alzheimer's disease [6]. DBS of the thalamic ventral intermediate nucleus (Vim) – i.e., Vim-DBS – is the primary surgical option of DBS for treating essential tremor. Essential tremor is the most common adult tremor disorder affecting up to 1% of adults over 40 years of age, and features attention tremor and uncontrollable shaking of the affected body part [7,8].

Despite the recognized clinical benefits of DBS, its therapeutic mechanisms on the disease-affected neural circuits are not fully understood [1,9]. In clinical setting, depending on specific diseases and symptoms, both low frequency (<100Hz) [10,11] and high frequency DBS (≥100Hz) [12,13] can be clinically effective. However, benefits from low frequency DBS are less commonly observed [14,15]. Since electrical pulses preferentially induce action potentials on nearby axons [16], the immediate effect of DBS on a given neuron is likely best explained by considering the simultaneous activation of all its synaptic inputs, and is further influenced by the ratio of excitatory to inhibitory inputs [9]. During low frequency DBS, a higher proportion of excitatory inputs may increase or synchronize the firing of action potentials [17], whereas a higher proportion of inhibitory inputs tends to decrease the neural firing rates [9]. When reacting to continuous pulse-trains of high frequency DBS, neurons are often observed to exhibit a transient firing rate response (whether a sudden increase or decrease), followed by a settling into a steady-state response of some kind [18,9,19]. This transition is likely due to a combination of factors such as axonal conduction failure and the time-course of synaptic depression [20,9,21]. Recently, a firing rate model representing neural activities of a single population of neurons was developed to replicate instantaneous firing rates of different nuclei of the basal ganglia and thalamus in response to various frequencies of DBS [22]. The model appropriately fitted the firing rate response data during low frequency Vim-DBS, but it deviated from observations during high frequency Vim-DBS [22]. An improved network modeling approach that incorporates the synaptic contributions of recurrent inhibitory and excitatory axonal processes can be more informative in capturing the neural response dynamics to varying frequencies of DBS. There have indeed been computational models on neural networks impacted by DBS [23,24,25,26,27]; however, these models mainly focus on simulating the DBS-induced dynamics of the local field potentials (LFP), and the fit to detailed single-neuron firing rate is lacking. To the best of our knowledge, there has been no neural network model that can accurately track the instantaneous firing rate from in-vivo human recordings during DBS.

We showed that modeling solely the excitatory effect of DBS is an insufficient approach in capturing the dynamics during high frequency Vim-DBS [22]. The network model emphasizing the dominant excitatory recurrent connections is known as a “Hebbian assembly” model [28], which

downplays the role of inhibitory nuclei [29,28,30]. Although a Hebbian network model is consistent with some experimental data (e.g., visual cortex [29,30]), the role of inhibitory nuclei is significant in many networks, e.g., hippocampus [31], basal ganglia [32], sensory cortex [33] and thalamus [34]. In a neural network featuring both recurrent excitation and feedback inhibition, the inhibitory nuclei stabilize the network when the excitatory subnetwork is unstable [35,31,28]. Such a network is known as an "inhibition-stabilized network" (ISN) [36,35]. The firing rate dynamics in ISNs were addressed in a theoretical model of the "Balanced Amplification" mechanism of a recurrent neural network [28]. In a Balanced Amplification network, the large amplification of excitation—caused by either strong external input or positive recurrent circuitry—is balanced by strong feedback inhibition [28]. Hence, the network remains robust and reaches steady state without too much delay [28]. In addition to balancing the effect of strong inputs, during weak inputs, the inhibitory nuclei are less activated, and this leads to a supralinear increase of neural firing rate [35]. The balancing effects of both strong and weak inputs were conceptualized as a "stabilized-supralinear network" [35], and were experimentally observed in ferret visual cortex neurons receiving visual stimuli with varying stimulation strengths [35]. Such a Balanced Amplification mechanism with inhibition-stabilized effects is ubiquitous in cortical networks because of the prevalence of cortical inhibitory interneurons [28,37], and should be also universal in general brain networks, e.g. cortical-subcortical networks [27,32,23], when the role of inhibitory nuclei is significant.

In this work, we developed a firing rate model of the neural network of Vim impacted by Vim-DBS. In our model, the Vim-network consists of recurrent connections among three neural groups: DBS-targeted Vim neurons, external excitatory nuclei and inhibitory nuclei. The external nuclei are mainly from thalamus, cerebellum and motor cortex [38,9,39,40,41,42]. The incorporation of an external excitatory feedback component to the model may allow the model to capture the indirect effects of thalamic-DBS as they recurrently propagate through the motor control network, away from and back towards the Vim [38,40]. An inhibitory feedback component may capture the contributions of the thalamic reticular nucleus, as well as intra-nucleus inhibitory interneurons [41,42]. We fitted the model parameters to the experimental single-unit recordings in Vim neurons of human patients with essential tremor, and the patients received DBS with varying stimulating frequencies (range 5 to 200Hz) [9]. To minimize the fitting error of the model relative

to the experimental data across all DBS frequencies, we developed a novel model parameter sequential optimization method that automatically and accurately finds the globally optimal solution. A globally optimal solution is important in fully fitting DBS experimental data, because the data features are distinct between low and high frequencies of DBS [9,22], and typical optimization methods focusing on a local solution [43,44,45,46,47] will be biased towards a single DBS data feature [22]. In this work, our optimization method incorporates two physiological features of the DBS data: (1) Focused Feature, stressing the Vim firing rate dynamics observed during high frequency Vim-DBS, which is more clinically effective for essential tremor [12,48,49]; and (2) Stabilized Feature, referring to the Vim firing rate dynamics across both low and high frequencies of Vim-DBS. The rate network model with the parameter optimization method can consistently and accurately fit the experimental data across a range of different DBS frequencies, including {5, 10, 20, 30, 50, 100, and 200Hz}. Our model accurately tracks the instantaneous firing rate of the Vim neurons receiving DBS. With our model, we observed the central role of inhibitory nuclei in explaining the dynamics in the initial large transient response during high frequency Vim-DBS [18,19,9]. We found that the Vim-circuitry can be characterized by the Balanced Amplification mechanism that stresses the critical role of the inhibitory nuclei in stabilizing the network during strong external drive, e.g., high frequency DBS.

Our rate network model and optimization method can be potentially extended to identify and study various brain neural circuits. Our model can also be potentially implemented to optimize the DBS frequency in a closed-loop control system used in clinics.

RESULTS

Firing rate network model

We developed a firing rate model of the Vim-network in patients with essential tremor (**Figure 1**). The model was fitted to the experimental single-unit recordings of human Vim neurons receiving DBS with different frequencies – {5, 10, 20, 30, 50, 100, and 200Hz} [9]. To optimize the model parameters, we developed a novel route optimization method to search for consistent

model parameters that accurately replicate the experimental data across different DBS frequencies.

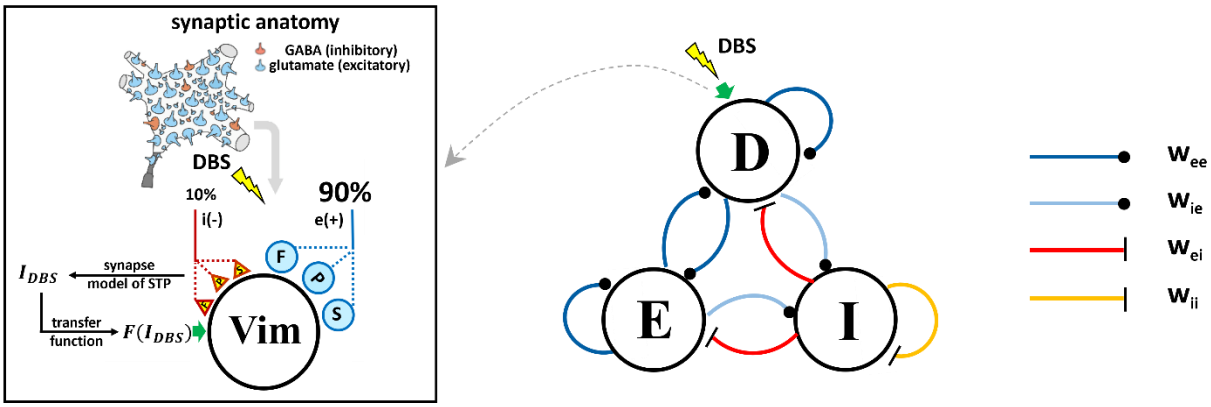

Figure 1. **Schematic illustration of the rate network model**

*The firing rate network model consists of 3 recurrent neural groups: "D" represents the ventral intermediate nucleus (Vim) neurons directly receiving DBS, "E" represents the external excitatory nuclei, and "I" represents the external inhibitory nuclei. w_{ei} represents the connectivity strength from inhibitory neurons to excitatory neurons; similar meanings for w_{ee}, w_{ie} and w_{ii}. The connection with a dot (respectively, a bar) represents excitation (respectively, inhibition). DBS is delivered to the neural group D, and we analyze the synaptic anatomic structure within group D, which consists of Vim neurons. A DBS pulse simultaneously activates all the synapses projecting to a Vim neuron in group D; 90% of these synapses are excitatory, and 10% of these synapses are inhibitory [9]. An excitatory synapse mainly projects glutamate neurotransmitter, and an inhibitory synapse mainly projects gamma-aminobutyric acid (GABA) neurotransmitter [9]. Excitatory (respectively, inhibitory) synapses consist of 3 types: "F" (facilitation), "P" (pseudo-linear)", and "S" (depression) [9]; see **Methods S3** for the proportions of the 3 synaptic types. We formulate the DBS-induced post-synaptic current (I_{DBS}) with the Tsodyks & Markram model of short-term synaptic plasticity (STP) ([50], **Methods S3**); I_{DBS} is then transferred (with a sigmoid function) to the corresponding firing rate dynamics $F(I_{DBS})$ (**Equation 1**). $F(I_{DBS})$ is the external DBS input into the rate network model.*

The rate network model of the Vim-DBS is illustrated in **Figure 1**. The model consists of three differential equations as stated below.

$$\begin{cases} \tau_e \frac{dr_D}{dt} = -\left(r_D - r_{D,0}\right) + [W\boldsymbol{r}]_D + F(I_{DBS}) \\ \tau_e \frac{dr_E}{dt} = -\left(r_E - r_{E,b}\right) + [W\boldsymbol{r}]_E \\ \tau_i \frac{dr_I}{dt} = -\left(r_I - r_{I,0}\right) + [W\boldsymbol{r}]_I \end{cases} \qquad \text{(Equation 1)}$$

where,

$$\boldsymbol{r} = \begin{pmatrix} r_D \\ r_E \\ r_I \end{pmatrix},$$

$$W = \begin{pmatrix} w_{DD} & w_{DE} & w_{DI} \\ w_{ED} & w_{EE} & w_{EI} \\ w_{ID} & w_{IE} & w_{II} \end{pmatrix} = \begin{pmatrix} w_{ee} & w_{ee} & -w_{ei} \\ w_{ee} & w_{ee} & -w_{ei} \\ w_{ie} & w_{ie} & -w_{ii} \end{pmatrix},$$

$$F(I_{DBS}) = \frac{c}{1+\exp\left[-s*(I_{DBS}-k)\right]};$$

undetermined parameters: $\Phi = \{w_{ee}, w_{ie}, w_{ei}, w_{ii}, \tau_i, \tau_e, r_{E,b}, c, s, k\}$

In **Equation 1**, neural group "D" represents the Vim neurons directly receiving DBS, neural group "E" represents the external excitatory nuclei, and neural group "I" represents the external inhibitory nuclei (**Figure 1**). The group "E" neurons are majorly the cerebellum dentate nucleus and the pyramidal cells of primary motor cortex (M1) deep layers (Layer 5 and 6) [38,9,39,40]. The group "I" neurons mostly consist of the thalamic reticular nucleus (TRN) and interneurons [41,9,42]. r_m ($m \in \{D, E, I\}$) represents the firing rate of the corresponding neural group. The baseline firing rate (with DBS–OFF) of Vim neurons ($r_{D,0}$) and the average firing rate of external inhibitory nuclei ($r_{I,0}$) were obtained from single-unit recordings reported in other studies [9,51]. We chose $r_{D,0}$ = 25Hz to be consistent with the human Vim experimental recordings in our previous work Milosevic et al. (2021) [9], and $r_{I,0}$ = 5Hz to be consistent with the experimental data recorded in both TRN (human) [9] and thalamic interneurons (mice) [51]. Since the external excitatory nuclei (group "E") are originated from multiple sources with highly variable firing rates [52,53], the corresponding baseline firing rate ($r_{E,b}$) is left as an unknown variable (**Equation 1**). In the experimental recordings from mice, the regular firing rate of cerebellum dentate nucleus ranged from 10 to 80Hz [52,54]. For M1 Layer 5 and 6 neurons in mice, the firing rate ranged from 10 to 60Hz [53,55]. Thus, we constrained $r_{E,b}$ in [10,70]Hz, and initialize it at $r_{E,b,0}$ = 40Hz.

In the rate network model, we use τ_e and τ_i to denote the excitatory and inhibitory time constants, respectively (**Equation 1**). Since Vim neurons are excitatory [9], the time constant of the neural group "D" was τ_e. In a firing rate model of a population of neurons, the time constant (τ) represents the changing speed of the firing rate in response to the post-synaptic current [24].

Generally, time constants in firing rate models were considered in the range of 0 to 30ms [24,56]. The rate model time constant is consistent with the membrane time constant [24], and generally, the time constant of the inhibitory neurons is larger than that of the excitatory neurons [9,57,58,59].

The matrix W (**Equation 1**) indicates strength of connectivity between different groups of neurons [28,60]. In matrix W, w_{pq} (for p,q belong to group "D", "E", "I") represents the connectivity strength from the neural group " q " to group " p ", and the +/- sign denotes the excitatory/inhibitory effect. The total network input into each neural group is computed as the matrix multiplication $W\boldsymbol{r} = ([W\boldsymbol{r}]_D, [W\boldsymbol{r}]_E, [W\boldsymbol{r}]_I)^T$, where $[W\boldsymbol{r}]_D$, $[W\boldsymbol{r}]_E$ and $[W\boldsymbol{r}]_I$ represent the inputs into group "D", "E" and "I", respectively (**Equation 1**).

For the Vim neurons directly receiving DBS (group "D"), we modeled the DBS-induced postsynaptic current (I_{DBS}) with the Tsodyks & Markram model [50] of short-term synaptic plasticity (STP) (**Methods S3**) in agreement with Milosevic et al. (2021) [9]; I_{DBS} is then transferred (with a sigmoid function) to the corresponding firing rate dynamics $F(I_{DBS})$ ([22], **Figure 1**, **Equation 1**). In the sigmoid transfer function $F(I_{DBS})$, c, s and k are the scale, shape and shift parameters, respectively (**Equation 1**).

The undetermined parameter set in the rate network model is $\Phi = \{w_{ee}, w_{ie}, w_{ei}, w_{ii}, \tau_i, \tau_e, r_{E,b}, c, s, k\}$ (see **Equation 1**). All rate model simulations were conducted with the time resolution of dt = 0.1ms.

Human experimental data processing and model fit

The model parameters in the rate network model (**Equation 1**) were estimated based on the experimental single-unit recordings of human Vim neurons in patients undergoing DBS surgery for essential tremor. While recording activity of an individual Vim neuron, DBS was applied with one of the stimulation frequencies {5, 10, 20, 30, 50, 100, and 200Hz}, with specific stimulation length {10, 5, 3, 2, 1, 5, and 2s}, respectively (see **Methods S1** for detailed data protocols which were already reported in our previous work [9]). We obtained 5~8 recordings during each frequency of DBS, and computed the instantaneous firing rate with a time histogram method based on these multiple recordings (**Methods S2**). The instantaneous firing rate was computed by convolving the experimentally recorded spike trains with an optimized Gaussian kernel that

best characterized the spikes using a Poisson process ([61,62], **Methods S2**, **Figure S1**). We concatenated the instantaneous firing rate of each DBS frequency, and optimized the consistent model parameters across different DBS frequencies (5 to 200Hz) ([22], **Methods S4.1**). In **Figure 2**, we showed the instantaneous firing rate calculated from experimental data, the results of our model fit, and the optimal model parameters.

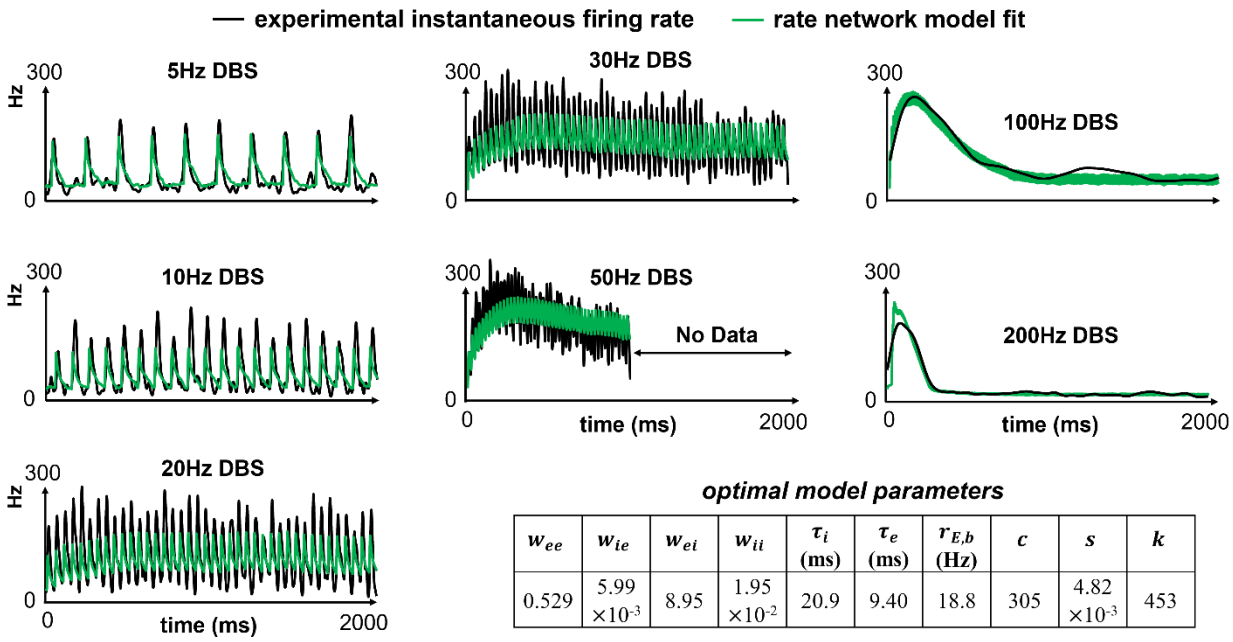

optimal model parameters

w_{ee}	w_{ie}	w_{ei}	w_{ii}	τ_i (ms)	τ_e (ms)	$r_{E,b}$ (Hz)	c	s	k
0.529	5.99×10^{-3}	8.95	1.95×10^{-2}	20.9	9.40	18.8	305	4.82×10^{-3}	453

Figure 2. Fitting rate network model to Vim-DBS in humans

*The firing rate network model is fitted to the experimental data recorded in the neurons in the ventral intermediate nucleus (Vim) of the human patients with essential tremor, during DBS of various stimulation frequencies (5 to 200Hz). For each frequency of DBS, we obtained 5 to 8 spike trains from experimental single-unit recordings in different patients, and compute the instantaneous firing rate using a time histogram method. In computing the experimental instantaneous firing rate, we implement an optimized Gaussian kernel that best characterized the Poisson process underlying the spiking data ([62], **Methods S2**). From the data of each DBS frequency, we present the model fit of the initial 2s; an exception is 50Hz DBS data, where the length of recording was ~1s. We compare the model fit (green line) with the experimental instantaneous firing rate (black line). The optimal model parameters (**Equation 1**) are obtained with our route optimization method (see text).* w_{pq} *(*$p, q \in \{i, e\}$*) is the connectivity strength (see **Figure 1** legend for specific descriptions).* τ_e *and* τ_i *are the excitatory and inhibitory time constants, respectively.* $r_{E,b}$ *is the baseline firing rate of the external excitatory nuclei (group* E*, **Figure 1**).* c*,* s *and* k *are the phenomenological parameters in the sigmoid transfer function* F *(**Equation 1**).*

As shown in **Figure 2**, the rate network model accurately reproduced the recorded firing rates across different DBS frequencies (5 to 200Hz). The model could capture both transient and steady-state firing rate responses to each frequency of DBS. In particular, for 100Hz and 200Hz DBS data, the model fit is almost identical to the experimental data; this improves the result from our previous model that incorporated a single population of Vim neurons, and ignored the recurrent connections with other nuclei ([22], **Figure S6**). For Vim-DBS, high-frequency DBS (100 to 200Hz) is more clinically effective than low-frequency DBS (<100Hz) [12,48,49]. Additionally, we optimized the model parameters based on the concatenated signal across different DBS frequencies (5 to 200Hz). When fitting a rate model to such DBS data with concatenated frequencies, the fit accuracy is consistent between observed and unobserved DBS frequencies (e.g., 130Hz, 160Hz; see Table 1 in Tian et al. (2023) [22]).

We quantitatively validated the model goodness of fit by computing the normalized mean squared error (NMSE) between the experimental instantaneous firing rate (reference) and the model generated firing rate. Since high frequency (100 to 200Hz) Vim-DBS is more clinically effective [12,48,49], we emphasized the high frequency DBS data, and defined the total fitting error (ER) for model validation:

$$ER = \frac{1}{3} * NMSE\ (5\ to\ 50Hz) + \frac{1}{3} * NMSE\ (100Hz) + \frac{1}{3} * NMSE\ (200Hz) \quad \text{(Equation 2)}$$

The NMSE(5 to 50Hz) represents the NMSE of the model fit to the concatenated data from DBS frequencies 5 to 50Hz. NMSE(100Hz) and NMSE(200Hz) were computed with data from the 100Hz and 200Hz DBS, respectively. For the rate network model fit shown in **Figure 2**, ER = 7.6%, with NMSE(5 to 50Hz) = 13.9%, NMSE(100Hz) = 3.2% and NMSE(200Hz) = 5.7%. See **Table S7** for the NMSE of the model fit to data from each DBS frequency. The optimal model parameters (**Figure 2**) were obtained with our route optimization method.

Route optimization method for model parameters

We developed a sequential optimization method for estimating undetermined parameters of the rate network model (**Equation 1**). This method, referred to as route optimization, effectively navigates the initial parameters in a route towards the globally optimal solution. During the optimization process, we reduce the mean squared errors (MSE) between the experimental

instantaneous firing rate and model predicted firing rates of the Vim neurons directly receiving DBS (group "D" in **Figure 1**) (**Methods S4**). Our aim was to find the optimal parameters that consistently fit the model to the instantaneous firing rate of Vim neurons receiving DBS across varying frequencies (5 to 200Hz). The undetermined parameter set Φ (**Equation 1**) is relatively high dimensional (dim = 10). In such a high dimensional parameter space, it is difficult to effectively find a globally optimal solution with local optimization methods [43,44,45,46,47]. Local optimization methods might be effective in exploitation, i.e., exploiting a local parameter range for the suitable local solution, but are not sufficient in exploration, i.e., exploring the whole parameter space for a globally appropriate solution [43,45,46]. An optimization method for finding the globally optimal solution should be effective in both exploitation and exploration.

In the route optimization method, we navigate an exploiting optimizer in a route that effectively explores the whole parameter space for the globally optimal solution. For the exploiting optimizer, we used the Nelder-Mead simplex method in the MATLAB custom function "*fminsearch*" [46,47]. The Nelder-Mead method is one of the most accurate gradient-approximating optimization methods, but is sensitive to the initial parameters and can be easily trapped in a local solution [43]. To develop the "route" in our optimization method, we first specify important features of interest, and define the optimization objective. For example, high frequency (100 and 200Hz) Vim-DBS is more clinically effective, thus firing rates corresponding to these frequencies are important to be replicated accurately. In this work, the *optimization objective* was to increase the accuracy in fitting high frequency DBS data, while maintaining a reasonable accuracy in fitting low frequency DBS data. To realize this optimization objective, we designed a set of objective functions to emphasize the important data features (e.g., "high frequency DBS"), and balance the fitting accuracy among all data features. By sequentially executing these objective functions, the route optimization method automatically navigates the exploiting Nelder-Mead optimizer to explore a route leading to the desired globally optimal solution that satisfies the optimization objective.

We have two main stages of optimization, namely, Global Stage and Refining Stage in the route optimization method (**Figure 3A**). Compared to Global Stage, Refining Stage stresses high frequency DBS data to a higher extent. Within each stage, the algorithm iterates between two

objective functions, referred to as "Pushing Function" and "Stabilizing Function" (**Figure 3B**, **Methods S4.2**), to estimate model parameters across different DBS frequencies. The objective functions are defined by the weighted sum of the MSE of individual DBS frequencies (**Methods S4.1**). We use the term "Focused Feature" to represent the higher weights of the MSE of high frequency (100Hz and 200Hz) DBS data (**Figure 3B**, **Methods S4.2**). Compared to Focused Feature, the term "Stabilized Feature" represents more balanced weights of the MSE of both low and high frequency DBS (**Figure 3B**, **Methods S4.2**). Focused Feature is important in increasing the fitting accuracy during high frequency DBS, which is underfitted in our previous study [22]. Stabilized Feature is important to keep the balance of the fitting accuracy across all DBS frequencies. Pushing Function emphasizes Focused Feature, whereas Stabilized Feature is stressed in Stabilizing Function (**Methods S4.2**). Within each iteration in either Global Stage or Refining Stage, the two objective functions were sequentially executed: from the Pushing Function, the output parameters (Φ_F , "F" represents Focused Feature) are the inputs to the Stabilizing Function (Φ_S , "S" represents Stabilized Feature) (**Figure 3B**). The output parameters of the Stabilizing Function will become the inputs to the Pushing Function in the next iteration (**Figure 3B**). This sequential process continues until the total fitting error (ER) (**Equation 2**) was sufficiently small, and satisfies an exit rule (**Figure 3B**, see **Equation 15** in **Methods S4.4** for details). The optimal parameters ($\Phi_{optimal}$) are the output of the route optimization method.

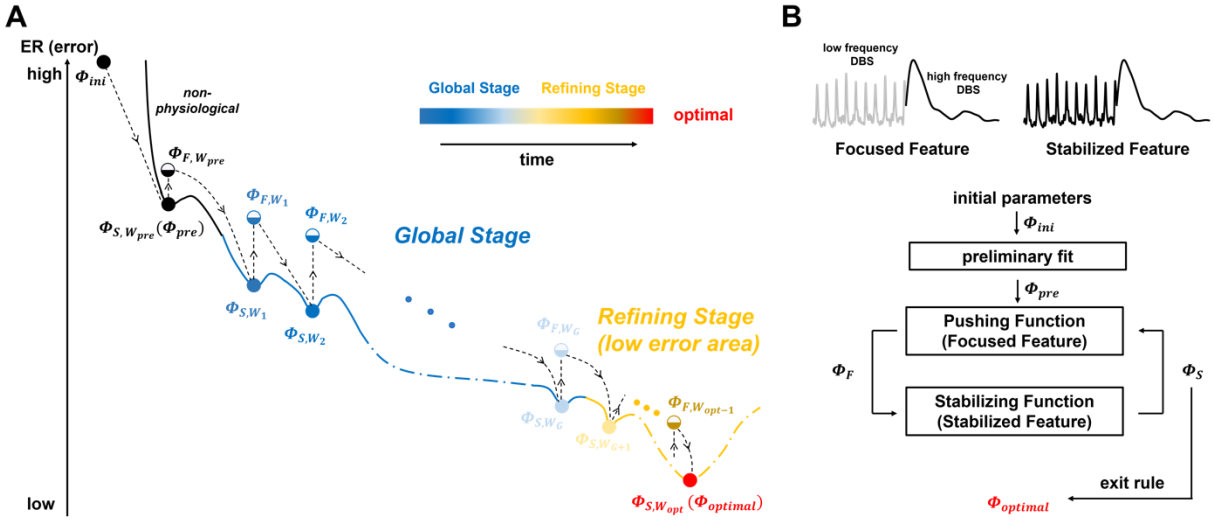

Figure 3. Schematic representation of the route optimization method

*(A) Schematic illustration of the route optimization method. The optimization objective was to minimize the model fitting error defined as ER in **Equation 2**; ER is essentially a weighted normalized mean squared error (NMSE) of the model fit. From a set of initial parameters (Φ_{ini}), we do a preliminary model fit and obtain the parameters Φ_{pre}. Φ_{ini} and Φ_{pre} are in the "non-physiological" parameter range, meaning that the fitting error (ER) with these parameters are very high. Φ_{pre} is the initial parameter set of the next model fit. The main stages of the optimization process are Global Stage and Refining Stage. Compared to Global Stage, Refining Stage stresses high frequency DBS data to a higher extent. The Global Stage explores the parameter space and leads the route towards a "low error area", which is exploited by the Refining Stage to locate the optimal parameters ($\Phi_{optimal}$). During the optimization process, Φ_F represents the model parameter set fitted to the Focused Feature (stressing high frequency DBS data), and Φ_S is fitted to the Stabilized Feature (balancing low and high frequency DBS data). W_i is the connectivity strength matrix (**Equation 1**) in Φ_{S,W_i}, which evolves to Φ_{F,W_i} in the next model fit. Φ_{S,W_i} is represented by a fully filled circle, and Φ_{F,W_i} is represented by a half-filled circle of the same color as Φ_{S,W_i}; this means that part of the parameters (i.e., W_i) are the same between Φ_{F,W_i} and Φ_{S,W_i}. Above is the color-coded timeline during the Global Stage and Refining Stage; the optimal parameter set ($\Phi_{optimal}$) is marked as red.*

*(B) Route optimization flow chart. The experimental data were from DBS in the ventral intermediate nucleus (Vim). The Focused Feature stresses the high frequency (100 & 200Hz) DBS data; high frequency Vim-DBS is more clinically effective for treating essential tremor. The Stabilized Feature balances the weights of low and high frequency DBS data. From the initial parameters (Φ_{ini}), we obtain Φ_{pre} after a preliminary model fit. Φ_{pre} enters the optimization main stages (Global Stage and Refining Stage, see (A)), which comprise iterations of two sequentially executed optimization objective functions: Pushing Function and Stabilizing Function. Pushing Function emphasizes the Focused Feature, and Stabilizing Function emphasizes the Stabilized Feature (**Methods S4.2**). In each sequential iteration, the output Φ_S of the Stabilizing Function is the initial parameter set for optimizing the Pushing Function, whose output Φ_F enters back to the Stabilizing Function to generate a new output. The sequential iterations terminate after an exit rule (i.e., small fitting error, see **Equation 15** in **Methods S4.4**) is satisfied, and the final output is the optimal parameter set $\Phi_{optimal}$ that minimizes ER (error).*

The route optimization starts with a set of initial parameters (Φ_{ini}), which came from previously reported parameters in other studies and a one-step fit with our previous single-ensemble model of the Vim neural group receiving DBS ([22], **Methods S4.3**). In particular, the initial connectivity strength parameters ($\{w_{ee}, w_{ie}, w_{ei}, w_{ii}\}$) were all set to 1. Starting from Φ_{ini}, we did a preliminary fit with Stabilizing Function, and the output parameters were Φ_{pre} (**Figure 3A and B**). The NMSE of the model fits with Φ_{ini} and Φ_{pre} were very large (>40%, **Table S5**); thus, the networks with these model parameters were considered to be in the "non-physiological"

regime, meaning that they were very different from the experimental data (**Figure 3A**). Φ_{pre} was also denoted as $\Phi_{S,W_{pre}}$ (**Figure 3A**); the subscript "S" represents that it was the output of Stabilizing Function emphasizing the Stabilized Feature, and the subscript "W_{pre}" stresses the strength of connectivity among neural groups in the network associated with Φ_{pre}. Starting from $\Phi_{S,W_{pre}}$, we performed a fit with Pushing Function, and obtained the output parameters $\Phi_{F,W_{pre}}$; the subscript "F" represents that it was the output of Pushing Function that emphasizes Focused Feature (**Figure 3A**). Note that in the fit for obtaining $\Phi_{F,W_{pre}}$ from $\Phi_{S,W_{pre}}$, we fixed the connectivity strength W_{pre}; and for $\Phi_{F,W_{pre}}$, this feature (fixed W_{pre}) is illustrated as a half-filled circle (**Figure 3A**). During the route optimization process, the connectivity strength was left unchanged in the Pushing Function to obtain Φ_F from Φ_S. Our purpose of this design was to increase the prediction robustness of the connectivity strength, which was the essential feature of a neural network. With the same connectivity strength W, the error of model fit with $\Phi_{F,W}$ was often larger than $\Phi_{S,W}$ (**Figure 3A**, **Table S5**) because $\Phi_{F,W}$ was obtained during fitting Focused Feature stressing part of the data (high frequency DBS). However, from $\Phi_{S,W}$ to $\Phi_{F,W}$, the model parameters always moved away from the local minimum, and the chances were opened up to explore the global minimum satisfying our optimization objective (**Figure 3A**). Thus, Pushing Function (on Focused Feature) "pushes" the model parameters away from the local solution towards the parameter range better representing Focused Feature, then Stabilizing Function (on Stabilized Feature) "stabilizes" the model parameters by fitting consistently across the whole data (i.e., Stabilized Feature) with high accuracy. Such sequential execution of Pushing Function and Stabilizing Function (**Figure 3B**) was the critical idea of the route optimization method in effectively finding the globally optimal solution.

Starting from Φ_{pre} , the 1st sequential optimization iteration is $\Phi_{pre} \rightarrow \Phi_{F,W_{pre}} \rightarrow \Phi_{S,W_1}$ (**Figure 3A and B**). The model fitting error (ER) of the network with parameters as the 1st iteration output (Φ_{S,W_1}) was 35.9%, which is far smaller than the networks in the non-physiological regime (**Figure 3A**, **Table S5**). Thus, we considered the network associated with Φ_{S,W_1} as physiologically meaningful, as well as each of the following network associated with a subsequent iteration output (Φ_{S,W_k} , $k \geq 2$); for these networks, ER decreases as the iteration number k increases

(**Figure 3A**, **Table S5**). In the physiological regime, starting from 1st iteration output (Φ_{S,W_1}), the route optimization proceeds as the sequential iteration number increases; the kth iteration ($k \geq 2$) is $\Phi_{S,W_{k-1}} \rightarrow \Phi_{F,W_{k-1}} \rightarrow \Phi_{S,W_k}$ (**Figure 3A**). The route optimization process in the physiological regime consists of two stages: Global Stage and Refining Stage (**Figure 3A**). The difference between the two stages is that, Refining Stage emphasizes the high frequency DBS data to a greater extent in the objective functions (**Methods S4.4**). Compared to Global Stage, in Refining Stage, the weight of high frequency DBS data was greater in both Pushing Function and Stabilizing Function (**Methods S4.4**). The purpose of Global Stage is to navigate the model parameters towards the appropriate range for fitting the data across all DBS frequencies; Refining Stage refines the parameter range obtained by Global Stage to further reduce the fitting error, in particular of the more clinically effective high frequency DBS data. The fitting error of the network associated with the final output of Global Stage (Φ_{S,W_G} , **Figure 3A**) was already small (ER = 9.5%, NMSE(100Hz) = 4.3%, NMSE(200Hz) = 10.6%); however, utilizing the objective functions of Global Stage solely would cause ER to stop decreasing (data not shown). Thus, we switched to Refining Stage to fully explore and exploit the "low error area" (**Figure 3A**) to minimize ER; after such local refinement, we finally found the desired globally optimal solution $\Phi_{optimal}$ (ER = 7.6%, NMSE(100Hz) = 3.2%, NMSE(200Hz) = 5.7%), which satisfied an exit rule (**Methods S4.4**) to quit the optimization iterations (**Figure 3B**). The optimal model fit the associated model parameters ($\Phi_{optimal}$) were shown in **Figure 2**.

The effective input to a neural group

As the route optimization algorithm evolves, the total fitting error (ER, **Equation 2**) decreases and the connectivity strength from inhibitory to excitatory groups (w_{ei}) increases (**Figure 4A**). w_{ei} and w_{ee} are the dominant connectivity strengths; the other two connectivity strengths (w_{ie} and w_{ii}) are far smaller in amplitude compared to w_{ei} and w_{ee} (**Figure 2**, **Table S5**). These connectivity features are important in identifying the network dynamics. The dynamics of a neural network is shaped by the effective transmission of the firing rate among interacting nuclei [60,63]. Such transmission is determined by two factors: (i) the connectivity strength modeled by W in **Equation 1** and (ii) the firing rate of the pre-synaptic nuclei. Thus, in our model, we formulate

the effective input [60] into a neural group as the product of connectivity strength and pre-synaptic firing rate. The "effective input matrix" of the Vim-network receiving DBS is defined in **Equation 3**,

$$S = \begin{pmatrix} s_{D\xi} & s_{DI} \\ s_{I\xi} & s_{II} \end{pmatrix} \qquad \text{(Equation 3)}$$

$$\textit{where } s_{DI} = \bar{r}_I w_{ei}\,,\ s_{D\xi} = (\bar{r}_E + \bar{r}_D) w_{ee},\ s_{II} = \bar{r}_I w_{ii},\ s_{I\xi} = (\bar{r}_E + \bar{r}_D) w_{ie}$$

The subscript "D" represents the Vim neural group directly receiving DBS; "E" and "I" represent the external excitatory and inhibitory nuclei, respectively (see **Equation 1** and **Figure 1**). The subscript "ξ" represents total input projected by excitatory neurons consisting of "D" and "E" groups of neurons. s_{mn} ($m \in \{D, I\}, n \in \{\xi, I\}$) indicates the effective input from group "n" to group "m", and it is equal to the product of the corresponding connectivity strength and pre-synaptic firing rate. w_{pq} ($p, q \in \{e, i\}$) is the modeled connectivity strength (**Equation 1**, **Figure 1**). The pre-synaptic firing rate $\bar{r}_n$ ($n \in \{D, E, I\}$) of the corresponding neural groups was calculated by averaging model generated firing rates across different DBS frequencies (5 to 200Hz).

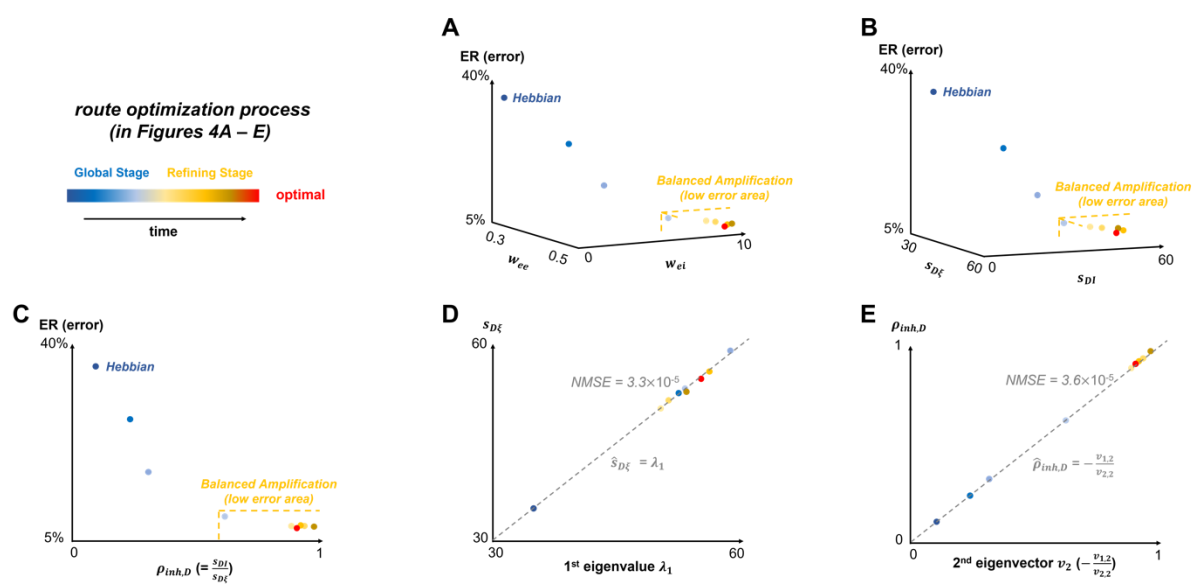

Figure 4. Evolution of the network mechanisms during the route optimization process

*Upper-left is the color-coded timeline during the main stages of the route optimization process (Global Stage and Refining Stage, see **Figure 3A**); the optimal network model fit is marked as red. "Hebbian" represents the modeled*

*network with the Hebbian mechanism, i.e., excitatory effects dominate inhibitory effects. In A-C, the model parameter set associated with the leftmost network is Φ_{B,W_1} (**Figure 3A**, **Table S4**), which is the start of the Global Stage. "low error area" represents the modeled networks with fitting error (ER, **Equation 2**) less than 10%. The modeled networks in the "low error area" are with the Balanced Amplification (BA) mechanism, i.e., balanced excitatory and inhibitory effects.*

*(A) Evolution of the dominant connectivity strengths (w_{ee} and w_{ei} , **Equation 1**, **Table S4**).*

*(B) Evolution of the effective synaptic inputs ($s_{D\xi}$ and s_{DI} , **Equation 3**, **Table S6**).*

*(C) Evolution of the inhibition strength ratio ($\rho_{inh,D}$, **Equation 4**). $\rho_{inh,D}$ defines the specific network mechanisms: low $\rho_{inh,D}$ characterizes a Hebbian network, whereas high $\rho_{inh,D}$ characterizes a Balanced Amplification network.*

*(D) 1st eigenvalue (λ_1) of the effective input matrix (**Equation 3**) and the excitatory effective input ($s_{D\xi}$). $s_{D\xi}$ is highly consistent with λ_1 in all modeled networks throughout the optimization process. "NMSE" is the normalized mean squared error; NMSE is computed based on the simple linear estimate $\hat{s}_{D\xi} = \lambda_1$ (gray dashed line).*

*(E) 2nd eigenvector ($\boldsymbol{v_2}$) of the effective input matrix (**Equation 3**) and the inhibition strength ratio ($\rho_{inh,D}$). $\rho_{inh,D}$ is highly consistent with $\boldsymbol{v_2} = \begin{pmatrix} v_{1,2} \\ v_{2,2} \end{pmatrix}$ in all modeled networks throughout the optimization process. NMSE is computed based on the simple linear estimate $\hat{\rho}_{inh,D} = -\frac{v_{1,2}}{v_{2,2}}$ (gray dashed line).*

For the Vim neurons receiving DBS (group "D"), as the route optimization algorithm evolves, the excitatory effective input ($s_{D\xi}$) remained relatively stable in the range 30 to 60(Hz), whereas the inhibitory effective input (s_{DI}) increased approximately from 0 to 55(Hz) (**Figure 4B**, **Table S6**). To quantify the differences in the effective inputs in the network models during the route optimization, we define the "inhibition strength ratio" (ρ_{inh}) as the ratio of inhibitory to excitatory effective inputs. For a certain neural group "m" in the network, we define

$$\rho_{inh,m} = \frac{s_{mI}}{s_{m\xi}}, \text{ where } m \in \{D, I\} \qquad \text{(Equation 4)}$$

As shown in **Figure 4C**, the fitting error (ER, **Equation 2**) decreased fast as $\rho_{inh,D}$ increased from ~ 0.1 to ~ 0.6, then ER stabilized and reached the minimum when $\rho_{inh,D} \sim 0.9$ (**Tables S5 and S6**). Initially, the very low $\rho_{inh,D}$ (~ 0.1) means that the excitatory effective input ($s_{D\xi}$) is dominant and the inhibitory effective input (s_{DI}) is negligible (**Figure 4C**). A network model that stresses the recurrent connections among excitatory nuclei is a "Hebbian network" [28,29,30]. The effect from inhibitory nuclei is negligible in a Hebbian network [29], or incorporated in the background noise [30]. Thus, we denote the network with small $\rho_{inh,D}$ (i.e., dominant excitatory

effects) as a Hebbian network (**Figure 4C**, **Table S6**). In the networks with relatively large $\rho_{inh,D}$ ($\rho_{inh,D} > 0.5$), the inhibitory effective input (s_{DI}) is an essential component of the network and is comparable with its excitatory counterpart. A network model with sufficient inhibitory effects in balancing excitatory effects is known as "Balanced Amplification network" [28], and we consider the network with $\rho_{inh,D} > 0.5$ (i.e., essential inhibitory effects) as a Balanced Amplification network (**Figure 4C**). The Balanced Amplification networks ($\rho_{inh,D} > 0.5$) constitute the "low error area" (**Figure 4C**), in which the model parameters fitted the experimental data with low error (ER < 10%, **Figure 4C**). The network with the optimal model parameters (**Figure 2**) is the typical Balanced Amplification network ($\rho_{inh,D} = 0.91$, marked as red color in **Figure 4C**), in which the excitatory and inhibitory effects are equally strong; this optimal network minimizes the model fitting error (ER = 7.6%, **Table S5**). To this end, we abbreviate "Balanced Amplification network" as "BA network" in text. **Video S1** illustrates the evolution of mechanisms during the route optimization process as shown in **Figure 4C** (specified in **Table S6**).

Network mechanisms in response to various frequencies of DBS

The network model variables were shown in **Figure 5** wherein we illustrated the data from two extremes of the DBS frequency spectrum (5 and 200Hz) studied in this work (see **Figures S2 to S5** for the model variables of data from all DBS frequencies). In **Figure 5**, we compared the model fitting results of two networks: (1) the typical Hebbian network with the lowest $\rho_{inh,D}$ shown in **Figure 4C**; and (2) the typical BA network, which is the network with the optimal model parameters (**Figure 2**). In the BA network, the model simulated firing rates (r_D, r_E and r_I, **Figure 5C – E**) and the predicted time constants (τ_e and τ_i , **Equation 1**, table in **Figure 2**) are all within the appropriate physiological ranges consistent with anatomical literature and experimental data [9,51,52,53,55,39,64,56]. For the firing rate of the external excitatory nuclei (r_E), during strong inputs, the bursting firing rate could be ~200Hz for both cerebellar [64] and M1 Layer 5 nuclei [39].

A Hebbian network (small $\rho_{inh,D}$) mainly consists of recurrent excitatory nuclei, and the excitation adds to itself through the passage of recurrent circuitry [28]. Thus, in a Hebbian network, the amplification of firing rate is non-robust in response to strong excitatory inputs. As shown in **Figure 5C** (5Hz Vim-DBS data), the peak amplitude of the modeled firing rate in the Hebbian

network was larger than that observed in the experimental data and that generated by the BA network; such error in the Hebbian network could be explained by the small ratio of s_{DI} to $s_{D\xi}$ (small $\rho_{inh,D}$; **Equation 4**), i.e., the inhibitory effective input (s_{DI}) was not strong enough to balance the excitatory effective input ($s_{D\xi}$). In contrast, $\rho_{inh,D}$ was large in the BA network, contributing to the more accurate fit to the experimental data (**Figure 5C**, 5Hz DBS data). See **Table S7** for the comparison of BA and Hebbian networks in terms of the NMSE of the model fit to data from each DBS frequency.

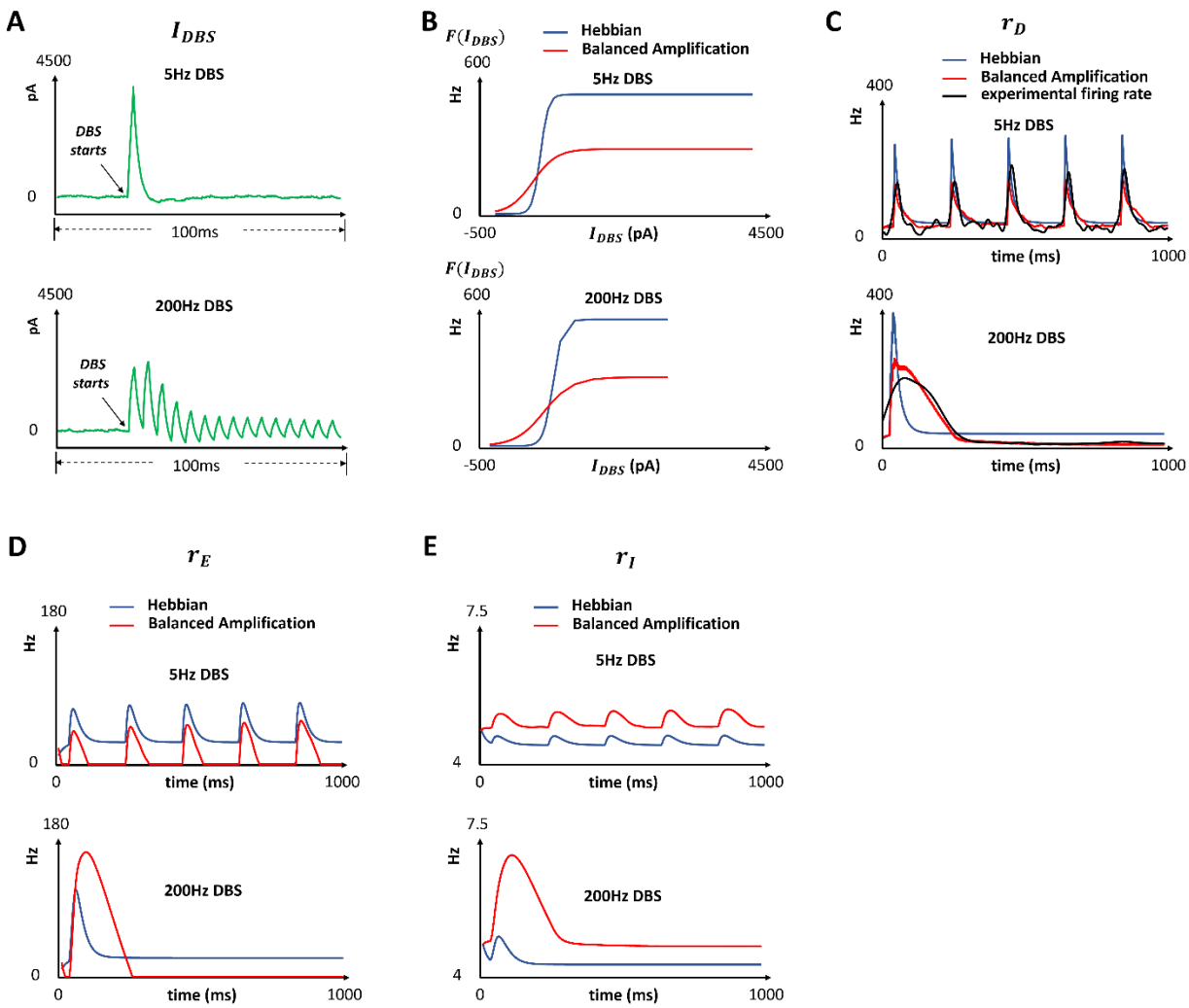

Figure 5. Variables of the rate network model with different mechanisms

*See **Equation 1** for the details of the variables. See the caption of **Figure 4** for the definitions of the two network mechanisms – Hebbian and Balanced Amplification.*

(A) Modeled DBS-induced postsynaptic current (I_{DBS}).

(B) Firing rate non-linear variability corresponding to I_{DBS} through a sigmoid transfer function ($F(I_{DBS})$).

(C) Firing rate of Vim (ventral intermediate nucleus) neurons directly receiving DBS (r_D).

(D) Firing rate of the external excitatory nuclei (r_E).

(E) Firing rate of the external inhibitory nuclei (r_I).

In the 200Hz Vim-DBS, there were two typical features: the initial large transient response (before ~300ms) and the steady state (beyond ~300ms) (**Figure 5C**, 200Hz DBS); the 100Hz Vim-DBS has similar features (**Figure 2**). As shown in **Figure 5C** (200Hz DBS), the modeled firing rate in the Hebbian network increased faster than that observed in both the experimental data and the BA network in the first ~50ms, although the input from the external excitatory nuclei (r_E) was consistent (between Hebbian and BA networks) in the first ~100ms (**Figure 5D**, 200Hz DBS). This indicates that the firing rate amplification was not robust in the Hebbian network. Thus, to fit a Hebbian network to experimental data, the optimization algorithm automatically adjusted model parameters to make r_E small in 100ms ~ 300ms (**Figure 5D**, 200Hz DBS) to eliminate the blow up of r_D; thus, the initial large transient period in the Hebbian network was shorter than that in the experimental data (**Figure 5C**, 200Hz DBS). Unlike the Hebbian network, r_E remained high in 100ms ~ 300ms in the BA network (**Figure 5D**, 200Hz DBS), contributing to a longer initial large transient period, which accurately matched the experimental data (**Figure 5C**, 200Hz DBS). In the BA network, the high r_E in 100ms ~ 300ms during 200Hz DBS (**Figure 5D**) was stabilized by the large $\rho_{inh,D}$, i.e., the strong excitatory drive was stabilized by the inhibitory inputs, and r_D remained robust during high r_E. In the BA network, the long initial transient response (in high frequency DBS data) was also consistent with the larger time constant of inhibitory neurons (τ_i , see the table in **Figure 2**), and it takes a longer time for the inhibitory neural group, compared to excitatory neurons, to impact network dynamics.

In fitting the steady state part of the 200Hz Vim-DBS experimental data (beyond 300ms), the BA network is identical to the experimental data, whereas the amplitude of the Hebbian network is larger than the BA network. The mismatch of the Hebbian network in fitting the steady state can be interpreted by the small $\rho_{inh,D}$, i.e., the weak inhibition-stabilized effect, which is insufficient in stabilizing the firing rate towards the experimental recordings. In the BA network,

the input from the recurrent excitatory circuitry ($s_{D\xi}$, **Equation 3**) was balanced by the strong inhibition-stabilized effect (large s_{DI}), and such balance was characterized by the large $\rho_{inh,D}$ (**Equation 4**), which quantified the optimal Balanced Amplification mechanism that accurately fitted the experimental data during 200Hz DBS, in both the initial large transient response (before ~300ms) and the steady state part of the firing rate (**Figure 5C**, 200Hz DBS).

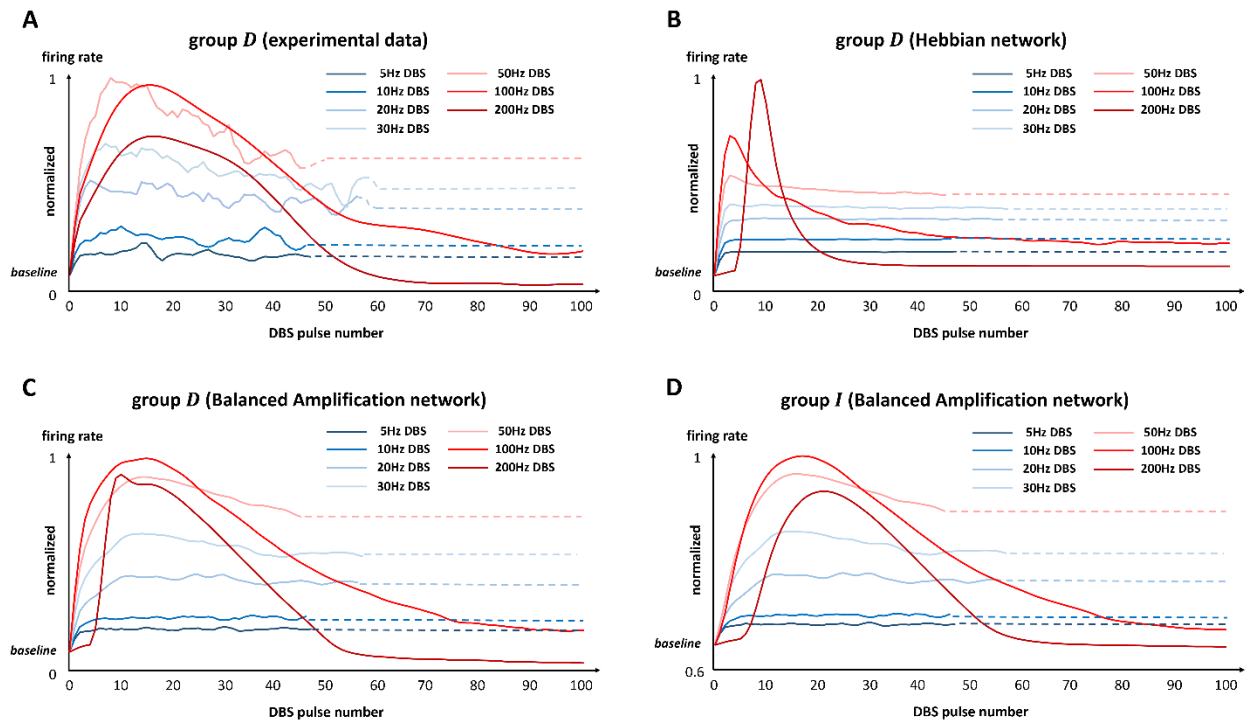

Figure 6. DBS impact as an external drive during different stimulation frequencies

In each plot, the firing rate at DBS pulse #i ($i \geq 1$) is defined as the mean firing rate in the $[(i-1)^{th}, (i+1)^{th}]$ inter-pulse-intervals, where "0th" represents the baseline firing rate before the onset of DBS; this baseline firing rate is used to define the firing rate at DBS pulse #0. The solid lines represent data and fits during clinical recordings, and the dashed lines represent the steady state estimations after clinical recordings. Note that in low frequency ($\leq$ 50Hz) DBS data and fits during clinical recording, the maximal number of DBS pulses is smaller, because the inter-pulse-interval is longer, and the total length of recording is restricted ($\leq$ 10s for each recording). In each plot, the firing rate is normalized to the maximum rate across all DBS frequencies.

*(A) Firing rate dynamics of the experimental recordings in the Vim neurons directly receiving DBS (group D, see **Figure 1**).*

*(B) Firing rate dynamics of the model simulations with the Hebbian mechanism (see caption of **Figure 4**), simulated on the Vim neurons directly receiving DBS.*

*(C) Firing rate dynamics of the model simulations with the Balanced Amplification mechanism (see caption of **Figure 4**) and the optimal model parameters (see **Figure 2**), simulated on the Vim neurons directly receiving DBS.*

*(D) Firing rate dynamics of the model simulations with the Balanced Amplification mechanism (see caption of **Figure 4**) and the optimal model parameters (see **Figure 2**), simulated on the inhibitory nuclei (group I, see **Figure 1**).*

The BA network was accurately fitted to the experimental data across all Vim-DBS frequencies from 5 to 200Hz (**Figure 2**, ER = 7.6%, **Table S7**). In low frequency Vim-DBS (5~50Hz), we observed large evoked activities in response to each DBS pulse (**Figure 2**). In order to clarify the underlying mechanism, we tracked the evolution of mean firing rate in inter-DBS-pulse intervals for each recorded frequency of DBS (5~200Hz) (**Figures 6A – D**); the mean firing rate is directly related to the metabolic energy consumed in physiological processes [65,66]. In **Figures 6A – D**, the firing rate at DBS pulse #i ($i \geq 1$) is defined as the mean firing rate in the $[(i-1)^{th}, (i+1)^{th}]$ inter-pulse-intervals, where "0th" represents the baseline firing rate before the onset of DBS; this baseline firing rate is used to define the firing rate at DBS pulse #0. During the DBS pulses of each frequency, we showed the firing rate dynamics of the Vim neurons in the experimental data (**Figure 6A**), the Hebbian network (**Figure 6B**), and the BA network (**Figure 6C**). In **Figure 6D**, we showed the firing rate dynamics of the external inhibitory nuclei in the BA network. One can observe that the BA network accurately tracked the firing rate of Vim-DBS during each DBS frequency (5 to 200Hz) (**Figures 6A and C**). However, the Hebbian network deviated from the experimental data, specifically for high frequency DBS data (100 and 200Hz). Both amplitude and duration of the initial large transient response (the initial ~60 DBS pulses) were not accurately estimated (**Figure 6A and B**).

We wanted to investigate the compatibility of our modeling strategy with different types of neuromodulations besides DBS. Another study observed the experimental single-unit recordings in ferret primary visual cortex (V1) neurons receiving visual stimuli with various stimulation strengths (e.g., different contrast or stimulus size) [35]. As the visual stimulation strength increased, the steady-state firing rate of ferret V1 neurons increased supralinearly when the stimuli were weak, and started to decrease when the stimuli became strong (see Figures 4 and S10 in Rubin et al. (2015) [35]). Such firing rate dynamics in response to various strengths of visual stimuli was modeled as a "stabilized-supralinear network": as external input strength increases, the network

transits from dominantly externally driven (supralinear increase in firing rate) to dominantly network driven, with the network inhibition stabilizing effect becomes increasingly dominant [35]. This stabilized-supralinear network model was developed and implemented to qualitatively represent the ferret V1 neuron experimental recordings in response to various strengths of visual stimuli [35]. In Vim-DBS (**Figure 6A**), during low frequency DBS (5 to 50Hz), the steady-state firing rate of the group D neurons (Vim neurons directly receiving DBS) increased as the DBS frequency increased; the steady-state firing rate decreased during high frequency DBS (100 and 200Hz). Such dynamics of experimental steady-state firing rate in response to various frequencies of DBS was accurately reproduced by our rate network model (**Figure 6A and C**). Besides, human Vim and ferret V1 neurons reacted similarly to the external drive (DBS and visual stimulation, respectively); as the strength of the external drive increased (increasing DBS frequency or visual stimulation strength), the steady-state firing rate first increased, then fast decreased. This implicates that our modeling framework – including the rate network model, optimization method and mechanism analysis strategy – can be generalizable to studying various brain circuits, receiving different types of external stimuli.

Network mechanisms with eigenvector interpretations

We implemented the inhibition strength ratio ($\rho_{inh,D}$) to quantify the network mechanisms; small $\rho_{inh,D}$ represents a Hebbian network, whereas large $\rho_{inh,D}$ represents a BA network. $\rho_{inh,D}$ was determined by the network excitatory and inhibitory effective inputs ($s_{D\xi}$ and s_{DI}) into the Vim neurons directly receiving DBS. Now the question is: Can $\rho_{inh,D}$ represent the network features identified by the effective input matrix S (**Equation 3**), which characterizes all nuclei in the modeled neural network? The answer is yes, substantiated by the following analysis in the perspective of the eigenvalues and eigenvectors of S.

The effective input matrix S consists of two eigenpairs: $(\lambda_1, \boldsymbol{v_1})$ and $(\lambda_2, \boldsymbol{v_2})$, where λ_j is the jth eigenvalue, and the associated j[th] eigenvector is $\boldsymbol{v_j} = \begin{pmatrix} v_{1,j} \\ v_{2,j} \end{pmatrix}$ ($j \in \{1,2\}$). We analyzed the evolution of eigenpairs during the route optimization process (**Methods S5**, **Table S6**). We found that the 1st eigenpair $(\lambda_1, \boldsymbol{v_1})$ characterized $s_{D\xi}$, i.e., the excitatory effective input into the Vim neurons directly receiving DBS; we deduced that $s_{D\xi} \approx \lambda_1$ (**Methods S5**, **Figure 4D**). The 2nd

eigenpair ($\lambda_2, \boldsymbol{v_2}$) characterized $\rho_{inh,D}$, i.e., the ratio of inhibitory to excitatory effective inputs to the Vim neurons directly receiving DBS (**Equation 4**); we deduced that $\rho_{inh,D} \approx -\frac{v_{1,2}}{v_{2,2}}$ (**Methods S5**, **Figure 4E**). We quantified these relationships by performing linear regression fits. The regression line of $s_{D\xi} \sim \lambda_1$ was

$$\hat{s}_{D\xi} = 0.988\lambda_1 + 0.400$$

where the 95% confidence interval of the slope and vertical intercept was, respectively [0.962, 1.015] and [-0.977, 1.777]. Thus, this regression line very closely approximated $\hat{s}_{D\xi} = \lambda_1$ (**Figure 4D**, gray dashed line). Similarly, the linear regression fit result of $\rho_{inh,D} \sim -\frac{v_{1,2}}{v_{2,2}}$ was

$$\hat{\rho}_{inh,D} = 1.008\left(-\frac{v_{1,2}}{v_{2,2}}\right) - 0.003$$

where the 95% confidence interval of the slope and vertical intercept was, respectively [1.002, 1.014] and [-0.007, 0.002]. This result was almost identical to $\hat{\rho}_{inh,D} = -\frac{v_{1,2}}{v_{2,2}}$ (**Figure 4E**, gray dashed line). For both simplified linear fits $\hat{s}_{D\xi} = \lambda_1$ and $\hat{\rho}_{inh,D} = -\frac{v_{1,2}}{v_{2,2}}$, the NMSE was smaller than 10^{-4} (**Figure 4D and E**). This demonstrated that the full variation of $s_{D\xi}$ (respectively, $\rho_{inh,D}$) was captured by λ_1 (respectively, $-\frac{v_{1,2}}{v_{2,2}}$) in all networks, with either Hebbian (small $\rho_{inh,D}$) or Balanced Amplification (large $\rho_{inh,D}$) features.

The analysis with the eigenvectors and linear regressions demonstrated that the network features of S can be characterized by $s_{D\xi}$ and $\rho_{inh,D}$. In **Figure 4D**, we saw that as the route optimization evolved, the dynamics of $s_{D\xi}$ was random, except for the initial smaller value. Despite such randomness in $s_{D\xi}$, its dynamics could always be perfectly captured by the 1st eigenvalue λ_1 ($\hat{s}_{D\xi} = \lambda_1$, **Figure 4D**). As the route optimization evolved, $\rho_{inh,D}$ first increased then stabilized around the optimal value at ~ 0.9; the dynamics of $\rho_{inh,D}$ could always be perfectly captured by the 2nd eigenvector $\boldsymbol{v_2}$ ($\hat{\rho}_{inh,D} = -\frac{v_{1,2}}{v_{2,2}}$, **Figure 4E**).

Comparison with a spiking network model

The spiking network model is a classical and ongoing approach for fitting the neural activity patterns in experimental data based on microscopic-level membrane potential dynamics [67,68]; the

commonly implemented Izhikevich spiking network model is a typical example [69,27]. We fitted the firing rate experimental data with an Izhikevich spiking network model (**Methods S6**) for testing the validity, and compared with our rate model.

Similar to the rate model, the Izhikevich spiking network model was on three groups of neurons: (1) 20 Vim neurons (excitatory) directly receiving DBS; (2) 100 excitatory neurons from the cerebellum [38,70]; (3) 40 inhibitory neurons from TRN [9,42]. Compared with the rate model, in the spiking model, we incorporated more physiological details of the DBS effects and synaptic connections (**Methods S6**). Besides the DBS activation of the synapses afferent into the Vim neurons (**Figure 1**), we incorporated the DBS effect of the axons efferent from the Vim neurons, and all synapses in the spiking network were characterized by the Tsodyks & Markram model [50,71] (**Methods S6**). The spiking model parameters were consistent with previous works [72,27,73,74], and were tuned so that for each group of neurons, the baseline firing rate (with DBS-OFF) was consistent with our rate network model (**Methods S6** and **Table S8**). All spiking model simulations were conducted with time resolution dt = 0.1ms (same as the rate model). We simulated the spiking model with different frequencies (5 ~ 200Hz) of Vim-DBS, and obtained the instantaneous firing rate of the Vim neurons with a time histogram, which was computed with the optimized Gaussian kernel (same as the rate model, see **Table S1**) on 20 simulated spike trains. We investigated two network mechanisms – Hebbian and Balanced Amplification – with the spiking network model; the two network mechanisms were characterized with the corresponding connectivity strength matrix W (**Equation 1** and **Table S4**), which is the result of our rate network model. To compare the two mechanisms, in the simulations, all the model parameters are the same except for the connectivity strength matrix W. We schematized the spiking network model mechanisms (**Figure 7A**), and showed their impacts on the Vim firing rate (**Figure 7C**); the spiking network model was compared with the rate network model (**Figure 7B and D**).

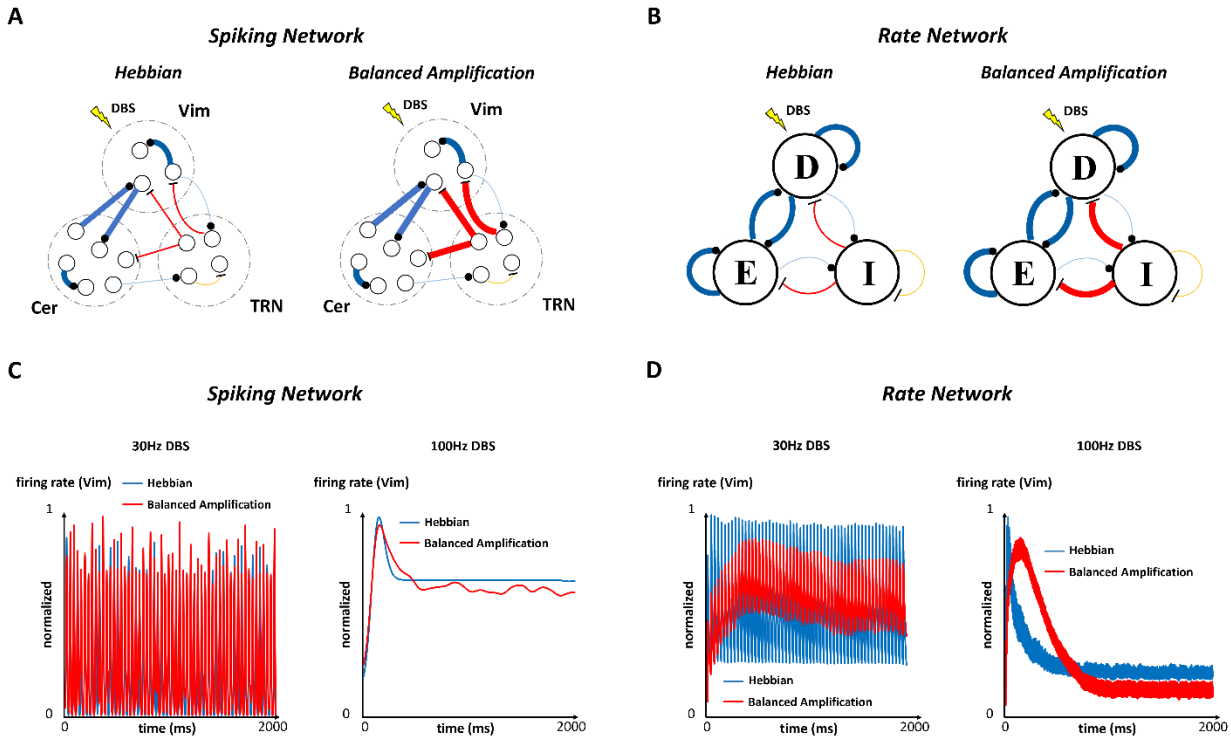

Figure 7. Compare network mechanisms in spiking and rate models

*(A – B) Schematic representation of the network mechanisms. The synaptic connection with a dot (respectively, a bar) represents an excitatory (respectively, inhibitory) synapse. The boldness of the connection represents the effective input, which is the multiplication of connectivity strength and firing rate (**Equation 3**). In the Hebbian mechanism, the ratio of inhibitory to excitatory effective inputs is low; such ratio is balanced (close to 1) in the Balanced Amplification mechanism.*

(A) Mechanisms of the spiking neuron network. The spiking network model consists of 3 groups of neurons: excitatory ventral intermediate nucleus (Vim) neurons directly receiving DBS, excitatory neurons in the cerebellum (Cer), and inhibitory neurons in the thalamic reticular nucleus (TRN).

(B) Mechanisms of the rate network. The firing rate network model consists of 3 neural groups: "D" represents the Vim neurons directly receiving DBS, "E" represents the external excitatory nuclei, and "I" represents the external inhibitory nuclei.

(C – D) Model simulations with the network mechanisms. We simulate the network models and present the results of Vim, receiving Vim-DBS of a typical low frequency (30Hz) and high frequency (100Hz), respectively. We present the results from two network mechanisms: Hebbian and Balanced Amplification, corresponding to the mechanism schematics in (A) and (B). In each plot, the results are normalized to the maximum rate across the two mechanisms.

(C) The spiking neuron network model simulations.

(D) The firing rate network model simulations.

The Izhikevich spiking network model qualitatively represented the underlying mechanisms and the results of the rate network model (**Figure 7C and D**). See **Figures S7 and S8** for the spiking model fits to data from different frequencies (5 ~ 200Hz) of Vim-DBS. In the spiking network, we found that the model fits with Hebbian and Balanced Amplification mechanisms were similar during 30Hz DBS (a typical low-frequency DBS), but distinct during 100Hz DBS (a typical high-frequency DBS) (**Figure 7C**); consistent comparisons were observed in the rate network (**Figure 7D**). The results from rate network model demonstrated that during low frequency ($\leq$ 50Hz) DBS, the fitting accuracy with the Hebbian network is comparable to the BA network; however, during high frequency ($\geq$ 100Hz) DBS, the Hebbian network deviates greatly from the BA network and experimental data (**Table S7, Figures 2 and S6**). These results implicated that the Balanced Amplification mechanism (strong inhibition-stabilized effect) is more evident during strong external inputs, e.g., a high frequency of DBS pulses. This was consistent with the previous result on the ferret V1 neurons receiving various strengths of visual stimuli; it was observed that the inhibition-stabilized effect dominated the network when the external visual stimuli were strong [35]. During 100Hz DBS, in the spiking network, compared with the Hebbian mechanism, the fit with Balanced Amplification mechanism showed smaller maximal firing rate, longer initial large transient response (~600ms) and lower steady state value (**Figure 7C**). All these results were consistent with the experimental data and the optimal rate network (**Figure 2** and **Figure 7D**). The consistency in network mechanisms between spiking and rate models demonstrated that the rate model effectively captured the Balanced Amplification mechanism underlying the Vim-network consisting of spiking neurons.

DISCUSSION

The firing rate network model with the parameter route optimization method could accurately reproduce the human experimental single-unit recordings in Vim neurons of essential tremor patients receiving intraoperative microstimulation during DBS surgery. With our route optimization method, we automatically found the consistent model parameters across different frequencies of DBS (5~200Hz). Our modeling and optimization method could also effectively

uncover and quantify the physiological mechanism underlying the neural network related to Vim. We found that the Vim-DBS experimental data could be effectively interpreted by the firing rate network model with a Balanced Amplification mechanism, in which the strong external drive and recurrent excitation were balanced by equally strong feedback inhibition. Our modeling, optimization and mechanism analysis strategies can be generalized in investigating other cortical-subcortical brain networks, receiving different types of external stimuli besides DBS.

The route optimization method is automatic and generalizable

We developed a model parameter optimization method that constructs a route leading to the globally optimal solution. Our route optimization method is automatic, in the sense that there is no hand-tuning of the model parameter set Φ (**Equation 1**) throughout the optimization process. Automatic parameter optimization is more accurate and efficient than the parameter hand-tuning, which is the most often implemented approach in analyzing network models or fitting data [75,32,76,77,67,78]. Although easy to explore, the parameter hand-tuning is often laborious and complicated to be implemented to find appropriate results [79], and depends heavily on prior knowledge which may not be optimal for the current data [32,76,78]. With an effective automatic optimization method, under appropriate biological constraints, we can efficiently find the optimal model parameters that accurately fit an experimental dataset, and these optimal parameters probably characterize the physiological underpinnings.

Our route optimization method can be implemented in a general setting, comprising a biological dataset and an appropriate network model. We first identify the physiological features of the dataset to be studied, and specify the optimization objective. In many scenarios, we can identify the dataset as consisting of two physiological features: one prominent feature that we currently focus on, and another secondary feature that may also be important. When fitting a network model to such a dataset, we can define its prominent feature as Focused Feature, define the weight-balance between its two features as Stabilized Feature, and proceed with the "pushing and stabilizing" strategy in this work (**Figure 3**) to design a route leading to the globally optimal model parameters that minimize fitting errors. There are also other scenarios wherein a different composition of physiological features – e.g., two prominent features or three features

– is appropriate for a specific dataset. In such scenarios, we can design the optimization route accordingly. For example, when fitting two prominent features, the definition of Focused Feature can alternate between the two features during the route optimization process. When fitting multiple ($\geq$3) features, we can stress each Focused Feature sequentially, while maintaining robustness by defining the weight-balance among all features as Stabilized Feature. Thus, the design of the route optimization is highly flexible to specific datasets and implementation goals. Compared with the traditional optimization methods – parameter hand tuning or one-step optimization (e.g., *fminsearch* in Matlab [46,47]), we anticipate that the route optimization method can be highly effective in finding the globally optimal solution – which characterizes physiological underpinnings – in a relatively high dimensional model parameter space.

Propagation to macroscopic network models and control systems

We developed a rate network model and implemented it in the neural circuits impacting thalamic Vim neurons receiving DBS. To implement the model in improving the clinical effects of DBS, it is essentially important to develop a closed-loop DBS control system that automatically adjusts the stimulation parameters to best suit each individual patient [80,81]. The closed-loop DBS control system consists of a biomarker as the feedback signal (e.g., oscillations in local field potentials (LFP) [82], power of electromyography (EMG) [83]), and a computational model that predicts the clinical state from such recordings in order to control DBS in a feedback-driven manner [43]. For example, in treating Parkinson's disease or essential tremor with closed-loop DBS control, the computational model can be a macroscopic network model of the disease-related physiological mechanism underlying the thalamocortical and cerebellar circuits [43,84]. In this work, we investigated the Vim-network with our model, and accurately reproduced the experimental recordings in Vim neurons across various DBS frequencies (5 to 200Hz). For further work, we can propagate the DBS impact on Vim neurons out towards their efferent target circuits, and build a macroscopic thalamocortical-cerebellar network model that quantifies the neurological disease mechanism. Finally, we will construct a closed-loop DBS control system based on the macroscopic thalamocortical-cerebellar network model, and clinically treat patients with neurological disorders by automatically adjusting DBS frequencies in continuous time.

Principle of identifying neural networks

With our rate network model, we explored the physiological mechanism underlying Vim-network in response to DBS. We found that the Vim-network can be identified as an inhibition-stabilized network with a Balanced Amplification mechanism, in which the strong external input and recurrent excitation are balanced by equally strong feedback inhibition. The Balanced Amplification mechanism (represented by the optimal model parameters) accurately fitted the experimental data, and was consistent across various DBS frequencies (5~200Hz) (**Figure 2**, **Table S7**). In contrast, the Hebbian mechanism (weak inhibition) was only appropriate for DBS data with low stimulation frequency ($\leq$50Hz), and missed the features of neural responses to high frequency ($\geq$100Hz) DBS (**Figure S4**, **Table S7**). Thus, in order to more fully identify the physiological components of the Vim-network, we need to fit the model consistently across data from a wide spectrum of DBS frequencies; if we confine the model fit within a small range of DBS frequencies, we probably identify the network mechanism erroneously. The same principle can be generalized to different types of neuromodulations: To identify the mechanism of a neural network with neuromodulation, we need to observe and model the neural response to a full range of the neuromodulation parameter, e.g., the frequency, pulse duration, or intensity of injected currents [85], focused ultrasound [86] and visual stimuli [35].

Relationship with other network models

Dynamics in neural networks emerge from the complex interplay among large number of neurons. The spiking network model is a direct simulation of the interaction among neurons, and the advantage of such a model lies in detecting neural activity patterns based on microscopic-level dynamics, including the membrane potential, activation probability of ion channels, and strength and variability of inter-neuron connections [27,87,68]. Typical examples of the spiking network model include leaky integrate-and-fire (LIF) [67], Izhikevich [69] and Hodgkin & Huxley types [87]. Despite the success of the spiking network model, its complexity and high dimensionality preclude the theoretical interpretation of network-level mechanisms [68,32].

The mean-field firing rate network model of neural populations has been the mainstay for interpreting mechanisms on the neural circuit level [68], including the E/I balance [28], connectivity among brain regions [88] and large-scale oscillations [84]. The typical and classical mean-field firing rate network model is of the Wilson-Cowan type [89], which assumes the homogeneity of neurons in one population [32,68]. Compared with the spiking network model, the mean-field firing rate network model reduces the complexity and dimensionality, and is more robust when tracking population-level dynamics and interactions [32,68]. Besides, the mean-field firing rate network model has fewer parameters, and is thus more efficient for implementation [43] and parameter automatic optimization [90].

Typically, a mean-field model assumes infinitely large populations, and is less sensitive to abrupt changes in inputs to local neurons [68]. In this work, we developed a mean-field firing rate network model that is consistent with the first principles, and also responds effectively to abrupt local input changes, i.e., the injection of DBS pulses to a local group of Vim neurons. We modeled the immediate impact of DBS pulses to the local Vim neural group as inducing synaptic release, and the synapses were characterized with the Tsodyks & Markram (TM) model [50]; such modeling of DBS effects is consistent with previously established works [9,22,91]. Our whole model consists of the local neural group directly receiving DBS, and its interactions with the external excitatory and inhibitory neural groups; the three neural groups are mutually recurrent (**Figure 1**).

Clinical implications and limitation of study

The DBS experimental data implemented in this work were recorded in a relatively short time scale ($\leq$10s) for each stimulation frequency (5~200Hz) (**Methods S1.2**). Within these short windows of recorded activity immediately following each DBS pulse, we divide the neuronal temporal response profile into an early-transient response and a latter steady-state response (**Figure 2**) within the context of clinical DBS for essential tremor. Since tremor symptoms often respond to stimulation on the scale of seconds, the relatively short timescales of our experimental data are nonetheless likely sufficient for initializing optimal DBS settings in clinics [83,92]. However, in considering the effects of stimulation at a longer time scale ($\geq$ minutes), the stimulated neurons may exhibit features of long term synaptic plasticity (LTP), which is the long-

term change in the synaptic connectivity or morphology [93,94,95]. LTP is widely observed in cortical neural circuits pertinent to memory [94] , learning [96] and neuromodulations [97,96], etc. The modeling on the possible LTP in long-duration DBS is part of our future work.

Our model extracts the main architecture of the Vim-circuitry, i.e., the Vim neural group and its recurrent connections with external excitatory and inhibitory neural groups. We incorporated all the external excitatory (resp., inhibitory) neurons into one group. Such structure blurred the details of these excitatory (resp., inhibitory) neurons. The connections among the neural groups were modeled by static synapses, i.e., the synaptic connectivity strength – e.g., w_{ei} (**Equation 1**) – is not time-varying. We incorporated synaptic plasticity (characterized by the Tsodyks & Markram model [50]) in the DBS-induced inputs into the Vim neural group, but synaptic plasticity was not considered within the modeled network. The purpose for such abstraction is to reduce the dimensionality and complexity of the rate model. We found that the robustness of model simulation decreases if incorporating more variables of synaptic connectivity into the model (data not shown). Thus, in the rate model, due to lack of synaptic plasticity within the modeled network, we didn't explicitly incorporate the DBS effect of the axons efferent from the Vim neurons towards external neural groups. The modeling of detailed synapses – including the DBS effect of Vim efferent axons – was incorporated in the spiking network model (**Methods S6**) that we developed to validate the rate network model. The results from the spiking network model were consistent with the rate network, showing that the abstraction in the rate model can capture the DBS-induced dynamics (**Figure 7**).

With our rate network model, we detected the Balanced Amplification mechanism – strong inhibition stabilization effects – underlying the Vim-circuitry. The Balanced Amplification mechanism is characterized by the high inhibition strength ratio (ρ_{inh} , **Equation 4**), meaning that the inhibitory synaptic inputs are comparable to or higher than the excitatory synaptic inputs. Experimental brain-slice works showed that during DBS of high frequency ($\geq$100Hz), the depression effect can be more evident for excitatory (glutamatergic) synapses than inhibitory (GABAergic) synapses [98,99]. These experimental results are consistent with the prediction from our model: in the simulations of both rate and spiking network models, we observed that the Balanced Amplification mechanism is more evident during high frequency DBS than low

frequency DBS (**Figure 7**). Clinical observations demonstrated that thalamic-DBS with low frequency (≤50Hz) exacerbates essential tremor [100,15]. The appearance of tremor – in the disease state and low frequency DBS – may indicate an underlying lack of Balanced Amplification mechanism (inhibition stabilization effects) of otherwise suppressed excitatory oscillations – these oscillations manifest as tremors in the muscles. Thus, a possible therapeutic mechanism of high frequency Vim-DBS is to restore the Balanced Amplification that could have perhaps been lost due to the disease state or low frequency DBS.

Conclusions

We developed a firing rate network model of the Vim-circuitry impacted by Vim-DBS, and a parameter route optimization method that automatically and effectively found the globally optimal model parameters fitted accurately and consistently across experimental data from various DBS frequencies (5~200Hz). Inferred from these optimal model parameters, we detected the Balanced Amplification mechanism characterizing the strong inhibition stabilization effects underlying the Vim-circuitry. Our modeling, parameter optimization and mechanism analysis strategies are generalizable to studying various brain circuits, receiving different types of neuromodulations besides DBS. The current work can be potentially extended to construct detailed macroscopic thalamocortical network models on quantifying different neurological disease mechanisms, and these future models will be implemented in closed-loop DBS control systems for automatic disease treatments.

METHODS

- S1 Human experimental data
  - S1.1 Ethical statement
  - S1.2 Data protocols and spike sorting
- S2 Time histogram with the optimized Gaussian kernel
- S3 The Tsodyks & Markram model of short-term synaptic plasticity (STP)
- S4 Route optimization method for model parameters
  - S4.1 Concatenate data from different frequencies of DBS

- S4.2 Data features and optimization objective functions
- S4.3 Preliminary fit
- S4.4 Main stages of the route optimization

- S5 Eigenpairs of the effective input matrix
- S6 The Izhikevich spiking network model

SUPPLEMENTARY INFORMATION

- **Supplementary Figures**

  - Figure S1. Compare different Gaussian time histogram kernel widths for computing instantaneous firing rate from DBS experimental data (*related to Methods S2*)
  - Figure S2. Modeled DBS-induced postsynaptic current into Vim (I_{DBS}) (*related to Figure 5*)
  - Figure S3. Optimal rate network model fit result for Vim-DBS human data ($F(I_{DBS})$, r_E and r_I) (*related to Figure 5*)
  - Figure S4. Hebbian rate network model fit result for Vim-DBS human data (r_D) (*related to Figure 5*)
  - Figure S5. Hebbian rate network model fit result for Vim-DBS human data ($F(I_{DBS})$, r_E and r_I) (*related to Figure 5*)
  - Figure S6. Single-ensemble rate model fit result for Vim-DBS human data (*related to Graphical abstract*)
  - Figure S7. Izhikevich spiking network model simulated firing rate for Vim neurons during Vim-DBS (Hebbian mechanism) (*related to Figure 7*)
  - Figure S8. Izhikevich spiking network model simulated firing rate for Vim neurons during Vim-DBS (Balanced Amplification mechanism) (*related to Figure 7*)
  - Figure S9. Tsodyks & Markram model used in the Izhikevich spiking network model (*related to Methods S6*)

- **Supplementary Tables**

- Table S1. The optimized Gaussian time histogram kernel for spiking data from each DBS frequency (*related to Methods S2*)
- Table S2. Tsodyks & Markram model parameters for synapses projected to one Vim neuron (*related to Equation 1)*
- Table S3. Weight vectors of data from different frequencies of DBS (*related to Methods S4*)
- Table S4. Evolution of the model parameters during the route optimization (3 significant digits) (*related to Figure 4 and Methods S4*)
- Table S5. Evolution of the model fitting errors during the route optimization (*related to Figure 3, Figure 4 and Methods S4*)
- Table S6. Evolution of the effective input matrix during the physiological range of route optimization (3 significant digits) (*related to Figure 4 and Methods S4*)
- Table S7. NMSE of the rate model fits to experimental data from each DBS frequency (*related to Equation 2)*
- Table S8. Parameters in the Izhikevich spiking network model (*related to Methods S6*)
- Table S9. Tsodyks & Markram model parameters used in the Izhikevich spiking network model (*related to Methods S6*)

- **Supplementary Video**
  - Video S1. Evolution of network mechanisms during route optimization (*related to Figure 4*)

ACKNOWLEDGEMENTS

We acknowledge AmirAli Farokhniaee for helpful discussions in simulating the Izhikevich spiking network model. This work was supported by Milad Lankarany's NSERC Discovery Grant (RGPIN-2020-05868), CIHR Project Grant and Brain Canada (Azrieli Foundation).

AUTHOR CONTRIBUTIONS

Conceptualization, Y.T. and M.L.; Rate model, Y.T. and M.L.; Optimization and data analysis, Y.T.; Result analysis, Y.T. and M.L.; Biological and clinical interpretations, Y.T., E.B., L.M., and M.L.; Validation with spiking model, Y.T., D.C., L.M., and M.L.; Data collection, S.K.K., M.H., A.M.L., W.D.H., and L.M.; Writing – original draft, Y.T. and M.L.; Writing – review & editing, Y.T., E.B., M.D.J., M.R.P., L.M., and M.L.; Funding acquisition, M.L.

DECLARATION OF INTERESTS

Suneil K. Kalia reports consulting fees from Boston Scientific, Medtronic, and Abbott. Andres M. Lozano reports consulting fees from Abbott, Boston Scientific, Medtronic, and Insightec. The remaining authors declare no competing interests.

METHODS

S1 Human experimental data

S1.1 Ethical statement

We used the same human experimental single-unit recordings which were previously published in Milosevic et al. [9]. Thus, the commitment to ethics policies have already been fulfilled [9]. All human experiments conformed to the guidelines set by the Tri-Council Policy on Ethical Conduct for Research Involving Humans and were approved by the University Health Network Research Ethics Board [9]. Moreover, each patient provided written informed consent prior to taking part in the studies [9].

S1.2 Data protocols and spike sorting

The human experimental data protocols and offline analysis methods were from Milosevic et al. (2021) [9]. Microelectrodes were used to both deliver DBS and perform single-unit recordings. DBS was delivered using 100µA and symmetric 0.3ms biphasic pulses (150µs cathodal followed by 150µs anodal) [9]. In this work, we used the single-unit recordings of the neurons in the thalamic ventral intermediate nucleus (Vim) of essential tremor patients, during various DBS frequencies (5 to 200Hz) in Vim. The single-unit recordings during {5, 10, 20, 30, 50, 100, and 200Hz} Vim-DBS are of length {10, 5, 3, 2, 1, 5, and 2s}, respectively; for each frequency of DBS, we did 5 to 8 recordings in different patients (total number of patients = 20). To obtain spikes from the single-unit recordings, we did offline analysis and spike template matching. For each single-unit recording, all the narrow stimulus artifacts were removed (0.5ms from the onset of a DBS pulse). Then the recordings were high pass filtered (≥300Hz) to better isolate the spikes, which were identified by the template matching using a principal component analysis method in Spike2 (Cambridge Electronic Design, UK).

S2 Time histogram with the optimized Gaussian kernel

After offline processing of the Vim single-unit recordings, we obtained 5 to 8 spike trains for each frequency of Vim-DBS ({5, 10, 20, 30, 50, 100, and 200Hz}), and computed the corresponding instantaneous firing rate with a time histogram method, which is a common practice in processing spiking data. However, people usually subjectively choose the kernel width for the time histogram, and ignore the underlying mechanisms generating the spikes [61]. In our work, we computed the instantaneous firing rate by convolving the spike trains with the optimized Gaussian kernel, which was obtained by the method in Shimazaki et al. (2007) [61] and Shimazaki et al. (2010) [62]. The optimized Gaussian kernel characterized the true Poisson process underlying the experimental spiking data [61,62]. Specifically, the optimized kernel minimized the mean integrated square error (MISE) from the true inhomogeneous Poisson point process underlying the experimental spike trains [61,62]. A time histogram kernel with small MISE could capture the abrupt firing rate fluctuations, while reducing the excessive overfitting [61,62]. From the spike trains recorded during each frequency of DBS, we computed the instantaneous firing rate with the optimized Gaussian kernel; see **Table S1** for the optimized kernel of the data from each DBS

frequency. The instantaneous firing rate with the optimized Gaussian kernel grasped the transient fluctuations very well, while the overfitting was prevented, in both 5Hz and 200Hz DBS data (**Figure S1**). Compared with the optimized Gaussian kernel, a larger kernel caused the instantaneous firing rate to deviate from the transient fluctuations, and a smaller kernel made the instantaneous firing rate exhibit excessive overfitting (**Figure S1**).

S3 The Tsodyks & Markram model of short-term synaptic plasticity (STP)

The external input into the Vim-network was the DBS-induced post-synaptic current (I_{DBS} , **Figure 1**, **Equation 1**), which was formulated with the Tsodyks & Markram (TM) model of short-term synaptic plasticity (STP) [50]. Thus, the immediate impact of DBS pulses was modeled as inducing synaptic release, and such modeling method is consistent with previously established works [9,22,91]. For the Vim neurons directly receiving DBS, we modeled that each neuron receives inputs from 500 synapses, with 90% excitatory synapses (N_{exc} = 450) and 10% inhibitory synapses (N_{inh} = 50) ([9], **Figure 1**, **Table S2**). We assumed that each DBS pulse generates one spike in each of these synapses simultaneously [9,22]. These DBS-evoked spikes were filtered by the TM model, generating the post-synaptic current, I_{DBS}, that was obtained by a linear combination of post-synaptic excitatory (I_{exc}) and inhibitory (I_{inh}) currents as follows:

$$I_{DBS}(t) = w_{exc}\, I_{exc}(t) - w_{inh} I_{inh}(t) \qquad \text{(Equation 5)}$$

where w_{exc} and w_{inh} denote the scaling weights of the excitatory and inhibitory currents, respectively (**Table S2**). I_{exc} (respectively, I_{inh}) is the total post-synaptic current from all excitatory (respectively, inhibitory) synapses; each synapse (excitatory or inhibitory) was modeled by the TM model of short-term synaptic plasticity:

$$\frac{du}{dt} = -\frac{u}{\tau_{facil}} + U(1-u^{-})\delta\left(t - t_{sp}\right) \qquad \text{(Equation 6)}$$

$$\frac{dm}{dt} = \frac{1-m}{\tau_{rec}} - u^{+}m^{-}\delta\left(t - t_{sp}\right) \qquad \text{(Equation 7)}$$

$$\frac{dI}{dt} = -\frac{I}{\tau_{s}} + Au^{+}m^{-}\delta(t - t_{sp}) \qquad \text{(Equation 8)}$$

where u is a utilization parameter, indicating the fraction of neurotransmitters ready for release into the synaptic cleft (due to calcium ion flux in the presynaptic terminal). The variable m indicates the fraction of resources remaining available after the neurotransmitter depletion

caused by neural spikes. We denote as u^- and m^- the corresponding variables just before the arrival of the spike; similarly, u^+ and m^+ refer to the moment just after the spike. The δ–function modeled the abrupt change upon the arrival of each presynaptic spike t_{sp}; for example, at $t = t_{sp}$ in **Equation 6**, u increases by $U(1-u^-)$, and $\delta(t-t_{sp}) = 0$ when $t \neq t_{sp}$. If there is no presynaptic activity (spike), u exponentially decays to zero; this decay rate is the facilitation time constant, τ_{facil} (**Equation 6**). In contrast to the increase of u upon the arrival of each presynaptic spike, m drops and then recovers to its steady state value (= 1); this recovery rate is given by the recovery time constant τ_{rec} (**Equation 7**). The competition between the facilitation (τ_{facil}) and recovery (τ_{rec}) time constants determined the dynamics of the synapse. In the TM model, U, τ_{facil}, and τ_{rec} were the parameters that determine the three types of the synapse: facilitation ("F"), pseudo-linear ("P"), and depression ("S") ([9], **Figure 1**, **Table S2**). In **Equation 8**, I is the post-synaptic current, A is the absolute response amplitude, and τ_s is the post-synaptic time constant (**Table S2**). We obtained I_{exc} (respectively, I_{inh}) by adding the post-synaptic currents from all excitatory (respectively, inhibitory) synapses. The TM model parameters in **Table S2** were chosen based on the previous modeling works on specific experimental datasets [9,101,102].

S4 Route optimization method for model parameters

S4.1 Concatenate data from different frequencies of DBS

We concatenated the experimental instantaneous firing rate of the data from different frequencies of Vim-DBS ({5, 10, 20, 30, 50, 100, and 200Hz}). Such "concatenated experimental instantaneous firing rate" was the reference for the model fit. As well, we concatenated the rate network model simulations during the above frequencies of DBS, and computed the mean squared error (MSE) between the concatenated signals (model simulation and reference). The purpose of minimizing MSE based on concatenated signals was to fit the model consistently across different DBS frequencies.

To be more specific, we used the sampling resolution dt = 0.1ms for all model simulations, and a simulated signal is denoted as $\boldsymbol{r}_{fq}(\Phi, \boldsymbol{t})$, which corresponds to a certain DBS frequency (fq)

and parameter set Φ (**Equation 1**); $\boldsymbol{r}_{fq}(\Phi, \boldsymbol{t}) = [\, r_{fq}(\Phi, t_1),\ \dots\ ,\ r_{fq}\left(\Phi, t_{N_{fq}}\right)]$ and N_{fq} is the total number of sampling time points. Similarly, the reference firing rate was sampled with the same resolution (dt = 0.1ms), and was denoted as $\boldsymbol{P}_{fq}(\boldsymbol{t}) = [\, P_{fq}(t_1),\ \dots\ ,\ P_{fq}\left(t_{N_{fq}}\right)]$; the corresponding MSE was computed as:

$$MSE_{fq}(\Phi) = \frac{1}{N_{fq}} \parallel \boldsymbol{r}_{fq}(\Phi, \boldsymbol{t}) - \boldsymbol{P}_{fq}(\boldsymbol{t}) \parallel^2 = \frac{1}{N_{fq}} \sum_{i=1}^{N_{fq}} [r_{fq}\ (\Phi\ , t_i) - P_{fq}(\ t_i)]^2 \quad \text{(Equation 9)}$$

Finally, the MSE between concatenated signals was the weighted sum across different DBS frequencies:

$$MSE_{conc}(\boldsymbol{g}, \Phi) = \sum_{fq} g_{fq} * \ MSE_{fq}(\Phi) \quad \text{(Equation 10)}$$

where fq ∈ {5, 10, 20, 30, 50, 100, and 200Hz}, g_{fq} is the weight of $MSE_{fq}(\Phi)$, and $\boldsymbol{g} = [g_{5Hz}, \dots, g_{200Hz}]$ is the weight vector, which depends on the specific purposes in the process of our route optimization method.

S4.2 Data features and optimization objective functions

Our *optimization goal* was to increase the accuracy in fitting data from high DBS frequencies (≥100Hz), while maintaining a reasonable accuracy in fitting data from low DBS frequencies (<100Hz). Thus, we stressed the data from high frequency of Vim-DBS, which is more clinically effective in treating essential tremor [12,48,49]. Based on our optimization goal, we defined two features of the Vim-DBS experimental instantaneous firing rate: Focused Feature and Stabilized Feature, whose differences were characterized by the weight vector $\boldsymbol{g}$ in computing MSE (**Equation 10**). Focused Feature emphasized the high frequencies (100Hz and 200Hz) DBS data, and the corresponding weights (g_{100Hz} and g_{200Hz}) were higher in computing the MSE (**Equation 10**, **Table S3**). Stabilized Feature, namely, balanced the weights of high frequency and low frequency DBS data in the MSE computations; i.e., $g_{fq \leq 50Hz}$ was not far from $g_{fq \geq 100\text{Hz}}$ (**Equation 10**, **Table S3**). Focused Feature is important in increasing the fitting accuracy (MSE) to data from high frequency of DBS, and Stabilized Feature is critical in fitting consistent model parameters across all DBS frequencies.

In order to fit Focused Feature or Stabilized Feature, we designed two types of optimization objective functions: Pushing Function and Stabilizing Function, which were the MSE

computations with different weight vectors $\boldsymbol{g}$ (**Equation 10**). Pushing Function emphasizes the Focused Feature, whereas Stabilized Feature is stressed in Stabilizing Function. The output parameters from each optimization objective function were obtained with the MATLAB custom function "fminsearch", which implemented the Nelder-Mead simplex method [46,47]. Pushing Function (on Focused Feature) "pushes" the model parameters away from the local solution towards the parameter range better representing Focused Feature, then Stabilizing Function (on Stabilized Feature) "stabilizes" the model parameters by fitting consistently across the whole data (i.e., Stabilized Feature) with high accuracy. Such sequential execution of Pushing Function and Stabilizing Function (**Figure 3B**) is the critical idea of the route optimization method in effectively finding the globally optimal solution.

S4.3 Preliminary fit

The undetermined parameter set to be optimized was $\Phi = \{w_{ee}, w_{ie}, w_{ei}, w_{ii}, \tau_i, \tau_e, r_{E,b}, c, s, k\}$ (**Equation 1**). The route optimization process started with a set of initial parameters $\Phi_{ini} = \{w_{ee,0}, w_{ie,0}, w_{ei,0}, w_{ii,0}, \tau_{i,0}, \tau_{e,0}, r_{E,b,0}, c_0, s_0, k_0\}$ (**Table S4**), which were determined as follows: (i) The initial connectivity strength parameters ($\{w_{ee,0}, w_{ie,0}, w_{ei,0}, w_{ii,0}\}$) were all set to be 1; (ii) $\{\tau_{i,0}, \tau_{e,0}, r_{E,b,0}\}$ were from the anatomical and experimental literature [103,9,52,54,53,104]; (iii) $\{c_0, s_0, k_0\}$ were from fitting the reference firing rate with our previous single-ensemble model of the Vim neural group receiving DBS [22]. Starting from the initial parameter set Φ_{ini} , we did a preliminary model fit based on Stabilized Feature (i.e., stressing data from both low and high frequencies of DBS), and the weight of each DBS frequency was given by the vector $\boldsymbol{g}_{pre}$ (**Equation 10**, **Table S3**). The output parameter set of this preliminary fit was denoted as Φ_{pre} (**Table S4**). The total fitting error (ER, **Equation 2**) with Φ_{ini} and Φ_{pre} were very large (>40%, **Table S5**), and model simulations with these two parameter sets were very different from the experimental data.

S4.4 Main stages of the route optimization

The preliminary fit result Φ_{pre} entered the main stages of the route optimization: Global Stage and Refining Stage (**Figure 3**). Global Stage explores the parameter space and finds the

appropriate parameter range with low total fitting error (ER, **Equation 2**); Refining Stage exploits the "low error area" attained by Global Stage, and finds the optimal parameter set $\Phi_{optimal}$ that minimizes the total fitting error (**Figure 3A**). Compared with Global Stage, Refining Stage stresses Focused Feature to a higher extent (**Table S3**). This design was compatible with our optimization goal in increasing the fitting accuracy of data from high frequencies of Vim-DBS (more clinically effective). Global Stage and Refining Stage comprise iterations of sequentially executed optimization objective functions – Pushing Function and Stabilizing Function (**Figure 3B**). Pushing Function in Global Stage (respectively, Refining Stage) was denoted as $J_{G,P}(\Phi)$ (respectively, $J_{R,P}(\Phi)$), and Stabilizing Function in Global Stage (respectively, Refining Stage) was denoted as $J_{G,S}(\Phi)$ (respectively, $J_{R,S}(\Phi)$); these four optimization objective functions were defined as follows:

$$J_{G,P}(\Phi) = MSE_{conc}(\boldsymbol{g}_{G,P}, \Phi) = \sum_{fq} g_{G,P,fq} * MSE_{fq}(\Phi) \quad \text{(Equation 11)}$$

$$J_{R,P}(\Phi) = MSE_{conc}(\boldsymbol{g}_{R,P}, \Phi) = \sum_{fq} g_{R,P,fq} * MSE_{fq}(\Phi) \quad \text{(Equation 12)}$$

$$J_{G,S}(\Phi) = MSE_{conc}(\boldsymbol{g}_{G,S}, \Phi) = \sum_{fq} g_{G,S,fq} * MSE_{fq}(\Phi) \quad \text{(Equation 13)}$$

$$J_{R,S}(\Phi) = MSE_{conc}(\boldsymbol{g}_{R,S}, \Phi) = \sum_{fq} g_{R,S,fq} * MSE_{fq}(\Phi) \quad \text{(Equation 14)}$$

where Φ is the undetermined parameter set (**Equation 1**); $\boldsymbol{g}_{G,P}$, $\boldsymbol{g}_{R,P}$, $\boldsymbol{g}_{G,S}$ and $\boldsymbol{g}_{R,S}$ are the corresponding weight vector (**Table S3**); fq is the DBS frequency and $fq \in$ {5, 10, 20, 30, 50, 100, and 200Hz}; MSE was computed by **Equations 9 and 10**.

In the 1st iteration of Global Stage, starting from Φ_{pre} (the preliminary fit result), we obtained $\Phi_{F,W_{pre}}$ by optimizing $J_{G,P}(\Phi)$ (**Equation 11**); in $\Phi_{F,W_{pre}}$ the subscript "F" represents that it is the output of a Pushing Function $J_{G,P}(\Phi)$ emphasizing Focused Feature, and the subscript "W_{pre}" stresses the connectivity strength features (**Equation 1**). Then, starting from $\Phi_{F,W_{pre}}$, we optimized $J_{G,S}(\Phi)$ (**Equation 13**) and obtained Φ_{S,W_1} . In Φ_{S,W_1} , the subscript "S" represents that it is the output of a Stabilizing Function $J_{G,S}(\Phi)$ emphasizing Stabilized Feature, and the subscript "W_1" shows that Φ_{S,W_1} is the output of 1st iteration of Global Stage. To conclude, the 1st iteration of Global Stage is summarized as $\Phi_{pre} \xrightarrow{J_{G,P}(\Phi)} \Phi_{F,W_{pre}} \xrightarrow{J_{G,S}(\Phi)} \Phi_{S,W_1}$. The kth iteration ($k \geq 2$) of Global Stage is summarized as $\Phi_{S,W_{k-1}} \xrightarrow{J_{G,P}(\Phi)} \Phi_{F,W_{k-1}} \xrightarrow{J_{G,S}(\Phi)} \Phi_{S,W_k}$. Note that when optimizing with Pushing Function $J_{G,P}(\Phi)$, the connectivity strength matrix W_{k-1} was always fixed. The

purpose of this design was to increase the prediction robustness of the connectivity strength, which was the essential feature of a neural network.

The end of Global Stage is denoted as Φ_{S,W_G} , which is also the start of Refining Stage. The kth iteration ($k \geq 1$) of Refining Stage is summarized as $\Phi_{S,W_{G+k-1}} \xrightarrow{J_{R,P}(\Phi)} \Phi_{F,W_{G+k-1}} \xrightarrow{J_{R,S}(\Phi)} \Phi_{S,W_{G+k}}$, where $J_{R,P}(\Phi)$ (**Equation 12**) is the Pushing Function, and $J_{R,S}(\Phi)$ is the Stabilizing Function (**Equation 14**). The final output of Refining Stage was the globally optimized model parameter set $\Phi_{optimal}$ with minimized fitting errors, which satisfied the optimization *exit rule*:

$$\text{ER} \leq 8\%,\ NMSE\ (100Hz) + NMSE\ (200Hz) \leq 9\% \qquad \text{(Equation 15)}$$

where ER is the "total fitting error" (**Equation 2**), and NMSE represents "normalized mean squared error". See **Tables S4 and S5** for the evolution of the model parameter set Φ and its fitting errors during the route optimization process, from the initial parameter set (Φ_{ini}) to the globally optimal solution ($\Phi_{optimal}$).

S5 Eigenpairs of the effective input matrix

We computed the eigenpairs – eigenvalues and the associated eigenvectors – of the effective input matrix S (**Equation 3**); **Table S6** showed the evolution of S and its eigenpairs during the route optimization process (as illustrated in **Figure 4D and E**). Suppose that the ith eigenpair of the effective input matrix S is ($\lambda_i, \boldsymbol{v_i} = \begin{pmatrix} v_{1,i} \\ v_{2,i} \end{pmatrix}$), and we deduced the following equations:

$$S\boldsymbol{v_1} = \begin{pmatrix} s_{D\xi} & s_{DI} \\ s_{I\xi} & s_{II} \end{pmatrix} \begin{pmatrix} v_{1,1} \\ v_{2,1} \end{pmatrix} = \lambda_1 \begin{pmatrix} v_{1,1} \\ v_{2,1} \end{pmatrix} \Rightarrow s_{D\xi} = -\frac{v_{2,1}}{v_{1,1}} s_{DI} + \lambda_1 \qquad \text{(Equation 16)}$$

$$S\boldsymbol{v_2} = \begin{pmatrix} s_{D\xi} & s_{DI} \\ s_{I\xi} & s_{II} \end{pmatrix} \begin{pmatrix} v_{1,2} \\ v_{2,2} \end{pmatrix} = \lambda_2 \begin{pmatrix} v_{1,2} \\ v_{2,2} \end{pmatrix} \Rightarrow s_{D\xi} = -\frac{v_{2,2}}{v_{1,2}} s_{DI} + \lambda_2 \qquad \text{(Equation 17)}$$

where λ_i ($i = 1,2$) is the ith eigenvalue of S, and $\boldsymbol{v_i} = \begin{pmatrix} v_{1,i} \\ v_{2,i} \end{pmatrix}$ ($i = 1,2$) is the ith eigenvector of S associated with λ_i .

During the route optimization process, we always observed that $\frac{\lambda_1}{s_{D\xi}} \approx 1$ and $\frac{v_{2,1}}{v_{1,1}} \approx 0$ (**Table S6**). This observation was consistent with **Equation 16**, which concretely showed that $s_{D\xi} \approx \lambda_1$ when $\frac{v_{2,1}}{v_{1,1}} \approx 0$. Thus, the excitatory effective input ($s_{D\xi}$) could mostly be represented by the 1st eigenvalue (λ_1). When observing the 2nd eigenpair ($\lambda_2, \boldsymbol{v_2}$) during the route optimization process,

we found that $\frac{\lambda_2}{s_{D\xi}}$ is always small; in fact, max ($\frac{\lambda_2}{s_{D\xi}}$) < 2% (**Table S6**). Thus, in analyzing the inhibition strength ratio $\rho_{inh,D} = \frac{s_{DI}}{s_{D\xi}}$ (**Equation 4**), we deduced the following equation from **Equation 17**:

$$\rho_{D,inh} = \frac{s_{DI}}{s_{D\xi}} = -\frac{v_{1,2}}{v_{2,2}}\left(1 - \frac{\lambda_2}{s_{D\xi}}\right) \approx -\frac{v_{1,2}}{v_{2,2}} \qquad \text{(Equation 18)}$$

because max ($\frac{\lambda_2}{s_{D\xi}}$) < 2% $\ll$ 1 (**Table S6**). Thus, the inhibition strength ratio $\rho_{inh,D}$ could mostly be represented by the 2nd eigenvector $\boldsymbol{v_2} = \begin{pmatrix} v_{1,2} \\ v_{2,2} \end{pmatrix}$.

S6 The Izhikevich spiking network model

We developed an Izhikevich spiking network model of the Vim-network, and compared its fitting results with our rate network model. The purpose was to validate our rate network model, and further discuss the network mechanism. The Izhikevich spiking network model was of 3 groups of neurons: (1) 20 Vim neurons (excitatory) directly receiving DBS; (2) 100 excitatory neurons from the cerebellum [38,70]; (3) 40 inhibitory neurons from the thalamic reticular nuclei (TRN) [9,42]. This setup of the Izhikevich model is consistent with the previous spiking models of the thalamocortical network [27,105]. The Izhikevich spiking network model equations are stated as follows,

$$v'_{nm} = 0.04v_{nm}^2 + 5v_{nm} + 140 - u_{nm} + I_{bias,m} + \xi_m + I_{DBS,m}\, k_m + \beta \sum_{q=1}^{3} I_{TM,mq} w_{mq} \qquad \text{(Equation 19)}$$

$$u'_{nm} = a_m(b_m v_{nm} - u_{nm}) \qquad \text{(Equation 20)}$$

$$\text{if } v_{nm} \geq \theta + \zeta_m \text{ , then } v_{nm} \leftarrow c_m \text{ , } u_{nm} \leftarrow u_{nm} + d_m \qquad \text{(Equation 21)}$$

$$W = \begin{pmatrix} w_{11} & w_{12} & w_{13} \\ w_{21} & w_{22} & w_{23} \\ w_{31} & w_{32} & w_{33} \end{pmatrix} = \begin{pmatrix} w_{ee} & w_{ee} & -w_{ei} \\ w_{ee} & w_{ee} & -w_{ei} \\ w_{ie} & w_{ie} & -w_{ii} \end{pmatrix} \qquad \text{(Equation 22)}$$

where m is the index of the neural group; m = 1, 2, 3 corresponds to the neural group Vim, cerebellum and TRN, respectively. Each group consists of N_m neurons, which are indexed by n = 1, 2, 3, ... ,N_m ; N_1 = 20, N_2 = 100, and N_3 = 40. The simulation of the Izhikevich spiking network model was performed with the Neural Simulation Tool (NEST) platform [106].

In **Equation 19**, v_{nm} is the membrane potential of the nth neuron in the mth group, and u_{nm} is the corresponding membrane recovery variable. $I_{bias,m}$ is the constant biased current injected to each neuron in the mth group, and ξ_m is the Gaussian white noise (see **Table S8** for its standard deviation). $I_{DBS,m}$ is the DBS-induced post-synaptic current into the mth group, with synapses characterized by the Tsodyks & Markram (TM) model [50,71]; k_m is a scaling parameter. $I_{DBS,1}$ represents the DBS activation of the synapses afferent into the Vim neurons (**Figure 1**). To be consistent with the input to the Vim-network in our rate model, $I_{DBS,1}$ was determined to be the same as the rate model input (I_{DBS}) in **Equation 1**. $I_{DBS,2}$ (respectively, $I_{DBS,3}$) represents the DBS effect of the axons efferent from the Vim neurons into the cerebellar neurons (respectively, neurons in TRN). $I_{DBS,2}$ and $I_{DBS,3}$ were simulated by the NEST built-in function "tsodyks2_synapse" [71,107]. We tuned the parameters in "tsodyks2_synapse" so that its simulation result is consistent with the Tsodyks & Markram synapses used in our rate model, across different DBS frequencies (5~200Hz) (**Table S9**, **Figures S2 and S9**). We tuned k_1 (the scaling of DBS effect of Vim afferent) so that the amplitude of the simulated DBS-evoked activities is consistent with our rate network model (**Figures 2 and S8**). The scaling parameters of DBS effect of Vim efferent (k_2 and k_3) are smaller than Vim afferent (k_1), because there is energy loss during the transmission on the axons efferent from Vim [108,109]. The ratio k_2/k_3 (i.e., the comparison of Vim efferent effects to cerebellum and TRN) is the same as the ratio of the corresponding connectivity strength (w_{ee}/w_{ie} , **Equations 1 and 22**).

In **Equation 19**, β is a scaling parameter of the effect of synaptic connections within the network. $I_{TM,mq}$ is the sum of TM-modeled post-synaptic currents induced by each spike of the group "q" neurons projecting to a group "m" neuron. $I_{TM,mq}$ was simulated by the NEST built-in function "tsodyks2_synapse" with parameters specified in **Table S9**. In the simulation of $I_{TM,mq}$, we used the sparse synaptic connection, which is commonly used in other spiking network models [110,77,111]. In our simulation, each neuron received synaptic inputs from 10% of Vim

neurons (excitatory), 10% of cerebellar neurons (excitatory), and 25% of TRN neurons (inhibitory). The connection probability from an inhibitory neuron was set to be higher, because an inhibitory neuron is generally dense in axons, and can project axons to distal neurons [112,41]. In the connectivity matrix W, w_{mq} represents the connectivity strength from the neural group "q" to group "m", and the +/- sign denotes the excitatory/inhibitory effect (**Equation 22**). The connectivity matrix W in the spiking model is the same as the rate model (**Equation 1**). In particular, in the spiking model, the two mechanisms – Hebbian and Balanced Amplification – are characterized by the connectivity strengths shown in **Table S4** (results of our rate model).

In **Equation 20**, u_{nm} is the membrane recovery variable, a_m is the time scale, and b_m is the sensitivity to the membrane potential v_{nm} . The neuron fires when v_{nm} reaches a fluctuating threshold $\theta + \zeta_m$ (**Equation 21**); θ = 30mV is the mean firing threshold, and ζ_m is the Gaussian white noise (see **Table S8** for its standard deviation). Immediately after the neuron fires, v_{nm} is reset to c_m , and u_{nm} is reset to $u_{nm} + d_m$ (**Equation 21**). The Izhikevich model parameters {a, b, c, d} for the neurons in each group were shown in **Table S8**; these parameters were chosen to be consistent with other works [27,74,73] . Other spiking model parameters were tuned so that for all neurons (Vim, cerebellum, or TRN), the simulated baseline firing rate (with DBS-OFF) was consistent with our rate network model.

REFERENCES

1. Boutet, A., Madhavan, R., Elias, G.J.B., Joel, S.E., Gramer, R., Ranjan, M., Paramanandam, V., Xu, D., Germann, J., Loh, A., et al. (2021). Predicting optimal deep brain stimulation parameters for Parkinson's disease using functional MRI and machine learning. Nature Communications *12*, 3043. 10.1038/s41467-021-23311-9.

2. Limousin, P., Krack, P., Pollak, P., Benazzouz, A., Ardouin, C., Hoffmann, D., and Benabid, A.-L. (1998). Electrical Stimulation of the Subthalamic Nucleus in Advanced Parkinson's Disease. New England Journal of Medicine *339*, 1105–1111. 10.1056/NEJM199810153391603.

3. Dallapiazza, R.F., Lee, D.J., Vloo, P.D., Fomenko, A., Hamani, C., Hodaie, M., Kalia, S.K., Fasano, A., and Lozano, A.M. (2019). Outcomes from stereotactic surgery for essential tremor. J Neurol Neurosurg Psychiatry *90*, 474–482. 10.1136/jnnp-2018-318240.

4. Hung, S.W., Hamani, C., Lozano, A.M., Poon, Y.-Y.W., Piboolnurak, P., Miyasaki, J.M., Lang, A.E., Dostrovsky, J.O., Hutchison, W.D., and Moro, E. (2007). Long-term outcome of bilateral pallidal deep brain stimulation for primary cervical dystonia. Neurology *68*, 457. 10.1212/01.wnl.0000252932.71306.89.

5. Menchón, J.M., Real, E., Alonso, P., Aparicio, M.A., Segalas, C., Plans, G., Luyten, L., Brunfaut, E., Matthijs, L., Raymakers, S., et al. (2019). A prospective international multi-center study on safety and efficacy of deep brain stimulation for resistant obsessive-compulsive disorder. Molecular Psychiatry, 1–14. 10.1038/s41380-019-0562-6.

6. Laxton, A.W., and Lozano, A.M. (2013). Deep Brain Stimulation for the Treatment of Alzheimer Disease and Dementias. World Neurosurgery *80*, S28.e1-S28.e8. 10.1016/j.wneu.2012.06.028.

7. Yousif, N., Mace, M., Pavese, N., Borisyuk, R., Nandi, D., and Bain, P. (2017). A Network Model of Local Field Potential Activity in Essential Tremor and the Impact of Deep Brain Stimulation. PLoS Comput Biol *13*. 10.1371/journal.pcbi.1005326.

8. Blomstedt, P., Sandvik, U., and Tisch, S. (2010). Deep brain stimulation in the posterior subthalamic area in the treatment of essential tremor. Movement Disorders *25*, 1350–1356.

9. Milosevic, L., Kalia, S.K., Hodaie, M., Lozano, A.M., Popovic, M.R., Hutchison, W.D., and Lankarany, M. (2021). A theoretical framework for the site-specific and frequency-dependent neuronal effects of deep brain stimulation. Brain Stimulation *14*, 807–821. 10.1016/j.brs.2021.04.022.

10. Xie, T., Vigil, J., MacCracken, E., Gasparaitis, A., Young, J., Kang, W., Bernard, J., Warnke, P., and Kang, U.J. (2015). Low-frequency stimulation of STN-DBS reduces aspiration and

freezing of gait in patients with PD. Neurology *84*, 415–420. 10.1212/WNL.0000000000001184.

11. Baizabal-Carvallo, J.F., and Alonso-Juarez, M. (2016). Low-frequency deep brain stimulation for movement disorders. Parkinsonism & Related Disorders *31*, 14–22. 10.1016/j.parkreldis.2016.07.018.

12. Earhart, G.M., Hong, M., Tabbal, S.D., and Perlmutter, J.S. (2007). Effects of Thalamic Stimulation Frequency on Intention and Postural Tremor. Exp Neurol *208*, 257–263. 10.1016/j.expneurol.2007.08.014.

13. Vaillancourt, D.E., Sturman, M.M., Verhagen Metman, L., Bakay, R. a. E., and Corcos, D.M. (2003). Deep brain stimulation of the VIM thalamic nucleus modifies several features of essential tremor. Neurology *61*, 919–925. 10.1212/01.wnl.0000086371.78447.d2.

14. Florin, E., Reck, C., Burghaus, L., Lehrke, R., Gross, J., Sturm, V., Fink, G.R., and Timmermann, L. (2008). Ten Hertz thalamus stimulation increases tremor activity in the subthalamic nucleus in a patient with Parkinson's disease. Clin Neurophysiol *119*, 2098–2103. 10.1016/j.clinph.2008.05.026.

15. Pedrosa, D.J., Auth, M., Eggers, C., and Timmermann, L. (2013). Effects of low-frequency thalamic deep brain stimulation in essential tremor patients. Experimental Neurology *248*, 205–212. 10.1016/j.expneurol.2013.06.009.

16. Ranck, J.B. (1975). Which elements are excited in electrical stimulation of mammalian central nervous system: A review. Brain Research *98*, 417–440. 10.1016/0006-8993(75)90364-9.

17. Eusebio, A., Chen, C.C., Lu, C.S., Lee, S.T., Tsai, C.H., Limousin, P., Hariz, M., and Brown, P. (2008). Effects of low-frequency stimulation of the subthalamic nucleus on movement in Parkinson's disease. Exp Neurol *209*, 125–130. 10.1016/j.expneurol.2007.09.007.

18. Milosevic, L., Kalia, S.K., Hodaie, M., Lozano, A.M., Popovic, M.R., and Hutchison, W.D. (2018). Physiological mechanisms of thalamic ventral intermediate nucleus stimulation for tremor suppression. Brain *141*, 2142–2155. 10.1093/brain/awy139.

19. Anderson, T., Hu, B., Pittman, Q., and Kiss, Z.H.T. (2004). Mechanisms of deep brain stimulation: an intracellular study in rat thalamus. J Physiol *559*, 301–313. 10.1113/jphysiol.2004.064998.

20. Zheng, F., Lammert, K., Nixdorf-Bergweiler, B.E., Steigerwald, F., Volkmann, J., and Alzheimer, C. (2011). Axonal failure during high frequency stimulation of rat subthalamic nucleus. J Physiol *589*, 2781–2793. 10.1113/jphysiol.2011.205807.

21. Rosenbaum, R., Zimnik, A., Zheng, F., Turner, R.S., Alzheimer, C., Doiron, B., and Rubin, J.E. (2014). Axonal and synaptic failure suppress the transfer of firing rate oscillations, synchrony and information during high frequency deep brain stimulation. Neurobiol Dis *62*, 86–99. 10.1016/j.nbd.2013.09.006.

22. Tian, Y., Murphy, M.J.H., Steiner, L.A., Kalia, S.K., Hodaie, M., Lozano, A.M., Hutchison, W.D., Popovic, M.R., Milosevic, L., and Lankarany, M. (2023). Modeling Instantaneous Firing Rate of Deep Brain Stimulation Target Neuronal Ensembles in the Basal Ganglia and Thalamus. Neuromodulation: Technology at the Neural Interface. 10.1016/j.neurom.2023.03.012.

23. Yousif, N., Mace, M., Pavese, N., Borisyuk, R., Nandi, D., and Bain, P. (2017). A Network Model of Local Field Potential Activity in Essential Tremor and the Impact of Deep Brain Stimulation. PLoS Comput Biol *13*. 10.1371/journal.pcbi.1005326.

24. Yousif, N., Bain, P.G., Nandi, D., and Borisyuk, R. (2020). A Population Model of Deep Brain Stimulation in Movement Disorders From Circuits to Cells. Front. Hum. Neurosci. *14*. 10.3389/fnhum.2020.00055.

25. Yu, Y., Wang, X., Wang, Q., and Wang, Q. (2020). A review of computational modeling and deep brain stimulation: applications to Parkinson's disease. Appl Math Mech *41*, 1747–1768. 10.1007/s10483-020-2689-9.

26. Schmidt, S.L., Brocker, D.T., Swan, B.D., Turner, D.A., and Grill, W.M. (2020). Evoked potentials reveal neural circuits engaged by human deep brain stimulation. Brain Stimul *13*, 1706–1718. 10.1016/j.brs.2020.09.028.

27. Farokhniaee, A., and Lowery, M.M. (2021). Cortical network effects of subthalamic deep brain stimulation in a thalamo-cortical microcircuit model. J Neural Eng *18*. 10.1088/1741-2552/abee50.

28. Murphy, B.K., and Miller, K.D. (2009). Balanced amplification: a new mechanism of selective amplification of neural activity patterns. Neuron *61*, 635–648. 10.1016/j.neuron.2009.02.005.

29. Douglas, R.J., Koch, C., Mahowald, M., Martin, K.A., and Suarez, H.H. (1995). Recurrent excitation in neocortical circuits. Science *269*, 981–985. 10.1126/science.7638624.

30. Goldberg, J.A., Rokni, U., and Sompolinsky, H. (2004). Patterns of Ongoing Activity and the Functional Architecture of the Primary Visual Cortex. Neuron *42*, 489–500. 10.1016/S0896-6273(04)00197-7.

31. Bekenstein, J.W., and Lothman, E.W. (1993). Dormancy of Inhibitory Interneurons in a Model of Temporal Lobe Epilepsy. Science *259*, 97–100. 10.1126/science.8093417.

32. van Albada, S.J., and Robinson, P.A. (2009). Mean-field modeling of the basal ganglia-thalamocortical system. I Firing rates in healthy and parkinsonian states. J Theor Biol *257*, 642–663. 10.1016/j.jtbi.2008.12.018.

33. Zhu, M., and Rozell, C.J. (2015). Modeling Inhibitory Interneurons in Efficient Sensory Coding Models. PLOS Computational Biology *11*, e1004353. 10.1371/journal.pcbi.1004353.

34. Min, B.-K. (2010). A thalamic reticular networking model of consciousness. Theoretical Biology and Medical Modelling *7*, 10. 10.1186/1742-4682-7-10.

35. Rubin, D.B., Van Hooser, S.D., and Miller, K.D. (2015). The stabilized supralinear network: A unifying circuit motif underlying multi-input integration in sensory cortex. Neuron *85*, 402–417. 10.1016/j.neuron.2014.12.026.

36. Tsodyks, M.V., Skaggs, W.E., Sejnowski, T.J., and McNaughton, B.L. (1997). Paradoxical Effects of External Modulation of Inhibitory Interneurons. J. Neurosci. *17*, 4382–4388. 10.1523/JNEUROSCI.17-11-04382.1997.

37. Thomson, A., and Lamy, C. (2007). Functional maps of neocortical local circuitry. Frontiers in Neuroscience *1*.

38. Marsden, J.F., Ashby, P., Limousin-Dowsey, P., Rothwell, J.C., and Brown, P. (2000). Coherence between cerebellar thalamus, cortex and muscle in man: Cerebellar thalamus interactions. Brain *123*, 1459–1470. 10.1093/brain/123.7.1459.

39. Oswald, M., Tantirigama, M., Sonntag, I., Hughes, S., and Empson, R. (2013). Diversity of layer 5 projection neurons in the mouse motor cortex. Frontiers in Cellular Neuroscience *7*.

40. Mease, R.A., and Gonzalez, A.J. (2021). Corticothalamic Pathways From Layer 5: Emerging Roles in Computation and Pathology. Front Neural Circuits *15*, 730211. 10.3389/fncir.2021.730211.

41. Murray Sherman, S., and Guillery, R.W. (2001). Chapter II - The Nerve Cells of the Thalamus. In Exploring the Thalamus, S. Murray Sherman and R. W. Guillery, eds. (Academic Press), pp. 19–58. 10.1016/B978-012305460-9/50016-2.

42. Guillery, R. w., and Harting, J.K. (2003). Structure and connections of the thalamic reticular nucleus: Advancing views over half a century. Journal of Comparative Neurology *463*, 360–371. 10.1002/cne.10738.

43. Grado, L.L., Johnson, M.D., and Netoff, T.I. (2018). Bayesian adaptive dual control of deep brain stimulation in a computational model of Parkinson's disease. PLOS Computational Biology *14*, e1006606. 10.1371/journal.pcbi.1006606.

44. Byrd, R., Schnabel, R., and Shultz, G. (1988). Approximate solution of the trust region problem by minimization over two-dimensional subspaces. Mathematical Programming *40*, 247–263. 10.1007/BF01580735.

45. Coleman, T.F., and Li, Y. (1994). On the convergence of interior-reflective Newton methods for nonlinear minimization subject to bounds. Mathematical Programming *67*, 189–224. 10.1007/BF01582221.

46. Nelder, J.A., and Mead, R. (1965). A Simplex Method for Function Minimization. Comput.J. *7*, 308–313. 10.1093/comjnl/7.4.308.

47. Lagarias, J.C., Reeds, J.A., Wright, M.H., and Wright, P.E. (1998). Convergence Properties of the Nelder--Mead Simplex Method in Low Dimensions. SIAM J. Optim. *9*, 112–147. 10.1137/S1052623496303470.

48. Reitz, S.C., Luger, S., Lapa, S., Eibach, M., Filmann, N., Seifert, V., Weise, L., Klein, J.C., Kang, J.-S., Baudrexel, S., et al. (2020). Comparing Programming Sessions of Vim-DBS. Frontiers in Neurology *11*.

49. Barbe, M.T., Reker, P., Hamacher, S., Franklin, J., Kraus, D., Dembek, T.A., Becker, J., Steffen, J.K., Allert, N., Wirths, J., et al. (2018). DBS of the PSA and the VIM in essential tremor: A randomized, double-blind, crossover trial. Neurology *91*, e543–e550. 10.1212/WNL.0000000000005956.

50. Tsodyks, M., Pawelzik, K., and Markram, H. (1998). Neural networks with dynamic synapses. Neural Comput *10*, 821–835. 10.1162/089976698300017502.

51. Charalambakis, N.E., Govindaiah, G., Campbell, P.W., and Guido, W. (2019). Developmental Remodeling of Thalamic Interneurons Requires Retinal Signaling. J. Neurosci. *39*, 3856–3866. 10.1523/JNEUROSCI.2224-18.2019.

52. Chabrol, F.P., Blot, A., and Mrsic-Flogel, T.D. (2019). Cerebellar Contribution to Preparatory Activity in Motor Neocortex. Neuron *103*, 506-519.e4. 10.1016/j.neuron.2019.05.022.

53. Benedetti, B., Dannehl, D., Janssen, J.M., Corcelli, C., Couillard-Després, S., and Engelhardt, M. (2020). Structural and Functional Maturation of Rat Primary Motor Cortex Layer V Neurons. Int J Mol Sci *21*, E6101. 10.3390/ijms21176101.

54. Baumel, Y., Jacobson, G., and Cohen, D. (2009). Implications of functional anatomy on information processing in the deep cerebellar nuclei. Frontiers in Cellular Neuroscience *3*.

55. Frandolig, J.E., Matney, C.J., Lee, K., Kim, J., Chevée, M., Kim, S.-J., Bickert, A.A., and Brown, S.P. (2019). The Synaptic Organization of Layer 6 Circuits Reveals Inhibition as a Major Output of a Neocortical Sublamina. Cell Rep *28*, 3131-3143.e5. 10.1016/j.celrep.2019.08.048.

56. Lim, S., McKee, J.L., Woloszyn, L., Amit, Y., Freedman, D.J., Sheinberg, D.L., and Brunel, N. (2015). Inferring learning rules from distributions of firing rates in cortical neurons. Nature Neuroscience *18*, 1804–1810. 10.1038/nn.4158.

57. Dufour, M.A., Woodhouse, A., Amendola, J., and Goaillard, J.-M. (2014). Non-linear developmental trajectory of electrical phenotype in rat substantia nigra pars compacta dopaminergic neurons. Elife *3*. 10.7554/eLife.04059.

58. Yang, S., Lin, W., and Feng, A.S. (2009). Wide-ranging frequency preferences of auditory midbrain neurons: Roles of membrane time constant and synaptic properties. Eur J Neurosci *30*, 76–90. 10.1111/j.1460-9568.2009.06797.x.

59. Economo, M.N., and White, J.A. (2012). Membrane Properties and the Balance between Excitation and Inhibition Control Gamma-Frequency Oscillations Arising from Feedback Inhibition. PLoS Comput Biol *8*, e1002354. 10.1371/journal.pcbi.1002354.

60. Sporns, O., Chialvo, D.R., Kaiser, M., and Hilgetag, C.C. (2004). Organization, development and function of complex brain networks. Trends in Cognitive Sciences *8*, 418–425. 10.1016/j.tics.2004.07.008.

61. Shimazaki, H., and Shinomoto, S. (2007). A method for selecting the bin size of a time histogram. Neural Comput *19*, 1503–1527. 10.1162/neco.2007.19.6.1503.

62. Shimazaki, H., and Shinomoto, S. (2010). Kernel bandwidth optimization in spike rate estimation. J Comput Neurosci *29*, 171–182. 10.1007/s10827-009-0180-4.

63. Babaeeghazvini, P., Rueda-Delgado, L.M., Gooijers, J., Swinnen, S.P., and Daffertshofer, A. (2021). Brain Structural and Functional Connectivity: A Review of Combined Works of Diffusion Magnetic Resonance Imaging and Electro-Encephalography. Front Hum Neurosci *15*, 721206. 10.3389/fnhum.2021.721206.

64. Womack, M.D., and Khodakhah, K. (2004). Dendritic Control of Spontaneous Bursting in Cerebellar Purkinje Cells. J Neurosci *24*, 3511–3521. 10.1523/JNEUROSCI.0290-04.2004.

65. Yi, G., and Grill, W.M. (2019). Average firing rate rather than temporal pattern determines metabolic cost of activity in thalamocortical relay neurons. Sci Rep *9*, 6940. 10.1038/s41598-019-43460-8.

66. Schölvinck, M.L., Howarth, C., and Attwell, D. (2008). The cortical energy needed for conscious perception. Neuroimage *40*, 1460–1468. 10.1016/j.neuroimage.2008.01.032.

67. Ponzi, A., and Wickens, J.R. (2012). Input Dependent Cell Assembly Dynamics in a Model of the Striatal Medium Spiny Neuron Network. Front. Syst. Neurosci. *6*. 10.3389/fnsys.2012.00006.

68. Schwalger, T., and Chizhov, A.V. (2019). Mind the last spike — firing rate models for mesoscopic populations of spiking neurons. Current Opinion in Neurobiology *58*, 155–166. 10.1016/j.conb.2019.08.003.

69. Izhikevich, E.M., and Edelman, G.M. (2008). Large-scale model of mammalian thalamocortical systems. PNAS *105*, 3593–3598. 10.1073/pnas.0712231105.

70. Stanziano, M., Golfrè Andreasi, N., Messina, G., Rinaldo, S., Palermo, S., Verri, M., Demichelis, G., Medina, J.P., Ghielmetti, F., Bonvegna, S., et al. (2022). Resting State Functional Connectivity Signatures of MRgFUS Vim Thalamotomy in Parkinson's Disease: A Preliminary Study. Frontiers in Neurology *12*.

71. Fuhrmann, G., Segev, I., Markram, H., and Tsodyks, M. (2002). Coding of temporal information by activity-dependent synapses. J Neurophysiol *87*, 140–148. 10.1152/jn.00258.2001.

72. Chelian, S.E., and Srinivasa, N. (2013). A spiking thalamus model for form and motion processing of images. In The 2013 International Joint Conference on Neural Networks (IJCNN), pp. 1–6. 10.1109/IJCNN.2013.6706790.

73. Izhikevich, E.M., Poggio, T.A., and Sejnowski, T.J. (2006). Dynamical Systems in Neuroscience: The Geometry of Excitability and Bursting (MIT Press).

74. Izhikevich, E.M. (2003). Simple model of spiking neurons. IEEE Trans. Neural Netw. *14*, 1569–1572. 10.1109/TNN.2003.820440.

75. Mastrogiuseppe, F., and Ostojic, S. (2018). Linking Connectivity, Dynamics, and Computations in Low-Rank Recurrent Neural Networks. Neuron *99*, 609-623.e29. 10.1016/j.neuron.2018.07.003.

76. Nakagawa, T.T., Woolrich, M., Luckhoo, H., Joensson, M., Mohseni, H., Kringelbach, M.L., Jirsa, V., and Deco, G. (2014). How delays matter in an oscillatory whole-brain spiking-neuron network model for MEG alpha-rhythms at rest. NeuroImage *87*, 383–394. 10.1016/j.neuroimage.2013.11.009.

77. Tang, J., Zhang, J., Ma, J., Zhang, G., and Yang, X. (2017). Astrocyte calcium wave induces seizure-like behavior in neuron network. Sci. China Technol. Sci. *60*, 1011–1018. 10.1007/s11431-016-0293-9.

78. Bhattacharya, S., Cauchois, M.B.L., Iglesias, P.A., and Chen, Z.S. (2021). The impact of a closed-loop thalamocortical model on the spatiotemporal dynamics of cortical and thalamic traveling waves. Sci Rep *11*, 14359. 10.1038/s41598-021-93618-6.

79. Amsalem, O., Eyal, G., Rogozinski, N., Gevaert, M., Kumbhar, P., Schürmann, F., and Segev, I. (2020). An efficient analytical reduction of detailed nonlinear neuron models. Nat Commun *11*, 288. 10.1038/s41467-019-13932-6.

80. Arlotti, M., Rosa, M., Marceglia, S., Barbieri, S., and Priori, A. (2016). The adaptive deep brain stimulation challenge. Parkinsonism Relat Disord *28*, 12–17. 10.1016/j.parkreldis.2016.03.020.

81. Little, S., Pogosyan, A., Neal, S., Zavala, B., Zrinzo, L., Hariz, M., Foltynie, T., Limousin, P., Ashkan, K., FitzGerald, J., et al. (2013). Adaptive deep brain stimulation in advanced Parkinson disease. Ann Neurol *74*, 449–457. 10.1002/ana.23951.

82. Priori, A., Foffani, G., Rossi, L., and Marceglia, S. (2013). Adaptive deep brain stimulation (aDBS) controlled by local field potential oscillations. Exp Neurol *245*, 77–86. 10.1016/j.expneurol.2012.09.013.

83. Yamamoto, T., Katayama, Y., Ushiba, J., Yoshino, H., Obuchi, T., Kobayashi, K., Oshima, H., and Fukaya, C. (2013). On-demand control system for deep brain stimulation for treatment of intention tremor. Neuromodulation *16*, 230–235; discussion 235. 10.1111/j.1525-1403.2012.00521.x.

84. van Albada, S.J., Gray, R.T., Drysdale, P.M., and Robinson, P.A. (2009). Mean-field modeling of the basal ganglia-thalamocortical system. II Dynamics of parkinsonian oscillations. J Theor Biol *257*, 664–688. 10.1016/j.jtbi.2008.12.013.

85. Lines, J., Martin, E.D., Kofuji, P., Aguilar, J., and Araque, A. (2020). Astrocytes modulate sensory-evoked neuronal network activity. Nat Commun *11*, 3689. 10.1038/s41467-020-17536-3.

86. Dallapiazza, R.F., Timbie, K.F., Holmberg, S., Gatesman, J., Lopes, M.B., Price, R.J., Miller, G.W., and Elias, W.J. (2018). Noninvasive neuromodulation and brain mapping with low intensity focused ultrasound. J Neurosurg *128*, 875–884. 10.3171/2016.11.JNS16976.

87. Giannari, A.G., and Astolfi, A. (2022). Model design for networks of heterogeneous Hodgkin–Huxley neurons. Neurocomputing *496*, 147–157. 10.1016/j.neucom.2022.04.115.

88. Bansal, K., Medaglia, J.D., Bassett, D.S., Vettel, J.M., and Muldoon, S.F. (2018). Data-driven brain network models differentiate variability across language tasks. PLOS Computational Biology *14*, e1006487. 10.1371/journal.pcbi.1006487.

89. Wilson, H.R., and Cowan, J.D. (1972). Excitatory and Inhibitory Interactions in Localized Populations of Model Neurons. Biophysical Journal *12*, 1–24. 10.1016/S0006-3495(72)86068-5.

90. Logiaco, L., Abbott, L.F., and Escola, S. (2021). Thalamic control of cortical dynamics in a model of flexible motor sequencing. Cell Reports *35*, 109090. 10.1016/j.celrep.2021.109090.

91. Farokhniaee, A., and McIntyre, C.C. (2019). Theoretical principles of deep brain stimulation induced synaptic suppression. Brain Stimul *12*, 1402–1409. 10.1016/j.brs.2019.07.005.

92. Herron, J.A., Thompson, M.C., Brown, T., Chizeck, H.J., Ojemann, J.G., and Ko, A.L. (2017). Chronic electrocorticography for sensing movement intention and closed-loop deep brain stimulation with wearable sensors in an essential tremor patient. J Neurosurg *127*, 580–587. 10.3171/2016.8.JNS16536.

93. Engert, F., and Bonhoeffer, T. (1999). Dendritic spine changes associated with hippocampal long-term synaptic plasticity. Nature *399*, 66–70. 10.1038/19978.

94. Kullmann, D.M., and Lamsa, K.P. (2007). Long-term synaptic plasticity in hippocampal interneurons. Nat Rev Neurosci *8*, 687–699. 10.1038/nrn2207.

95. Paulsen, O., and Sejnowski, T.J. (2000). Natural patterns of activity and long-term synaptic plasticity. Curr Opin Neurobiol *10*, 172–179.

96. Chiu, C.Q., Barberis, A., and Higley, M.J. (2019). Preserving the balance: diverse forms of long-term GABAergic synaptic plasticity. Nat Rev Neurosci *20*, 272–281. 10.1038/s41583-019-0141-5.

97. Palacios-Filardo, J., and Mellor, J.R. (2019). Neuromodulation of hippocampal long-term synaptic plasticity. Current Opinion in Neurobiology *54*, 37–43. 10.1016/j.conb.2018.08.009.

98. Steiner, L.A., Tomás, F.J.B., Planert, H., Alle, H., Vida, I., and Geiger, J.R.P. (2019). Connectivity and Dynamics Underlying Synaptic Control of the Subthalamic Nucleus. J. Neurosci. *39*, 2470–2481. 10.1523/JNEUROSCI.1642-18.2019.

99. Spix, T.A., Nanivadekar, S., Toong, N., Kaplow, I.M., Isett, B.R., Goksen, Y., Pfenning, A.R., and Gittis, A.H. (2021). Population-specific neuromodulation prolongs therapeutic benefits of deep brain stimulation. Science *374*, 201–206. 10.1126/science.abi7852.

100. Kuncel, A.M., Cooper, S.E., Wolgamuth, B.R., and Grill, W.M. (2007). Amplitude- and Frequency-Dependent Changes in Neuronal Regularity Parallel Changes in Tremor With Thalamic Deep Brain Stimulation. IEEE Transactions on Neural Systems and Rehabilitation Engineering *15*, 190–197. 10.1109/TNSRE.2007.897004.

101. Wang, Y., Markram, H., Goodman, P.H., Berger, T.K., Ma, J., and Goldman-Rakic, P.S. (2006). Heterogeneity in the pyramidal network of the medial prefrontal cortex. Nat Neurosci *9*, 534–542. 10.1038/nn1670.

102. Markram, H., Muller, E., Ramaswamy, S., Reimann, M.W., Abdellah, M., Sanchez, C.A., Ailamaki, A., Alonso-Nanclares, L., Antille, N., Arsever, S., et al. (2015). Reconstruction and Simulation of Neocortical Microcircuitry. Cell *163*, 456–492. 10.1016/j.cell.2015.09.029.

103. Landisman, C.E., Long, M.A., Beierlein, M., Deans, M.R., Paul, D.L., and Connors, B.W. (2002). Electrical Synapses in the Thalamic Reticular Nucleus. J. Neurosci. *22*, 1002–1009. 10.1523/JNEUROSCI.22-03-01002.2002.

104. Dura-Bernal, S., Neymotin, S.A., Suter, B.A., Dacre, J., Schiemann, J., Duguid, I., Shepherd, G.M., and Lytton, W.W. (2022). Multiscale model of primary motor cortex circuits reproduces in vivo cell type-specific dynamics associated with behavior. Preprint at bioRxiv, 10.1101/2022.02.03.479040 10.1101/2022.02.03.479040.

105. McCormick, D.A. (2017). Thalamocortical Networks. In Handbook of Brain Microcircuits, G. M. Shepherd, S. Grillner, G. M. Shepherd, and S. Grillner, eds. (Oxford University Press), p. 0. 10.1093/med/9780190636111.003.0009.

106. Gewaltig, M.-O., and Diesmann, M. (2007). NEST (NEural Simulation Tool). Scholarpedia *2*, 1430. 10.4249/scholarpedia.1430.

107. Tsodyks, M.V., and Markram, H. (1997). The neural code between neocortical pyramidal neurons depends on neurotransmitter release probability. Proceedings of the National Academy of Sciences *94*, 719–723. 10.1073/pnas.94.2.719.

108. Harris, J.J., Jolivet, R., and Attwell, D. (2012). Synaptic energy use and supply. Neuron *75*, 762–777. 10.1016/j.neuron.2012.08.019.

109. Chamberlain, K.A., and Sheng, Z.-H. (2019). Mechanisms for the maintenance and regulation of axonal energy supply. J Neurosci Res *97*, 897–913. 10.1002/jnr.24411.

110. Brunel, N. (2000). Dynamics of Sparsely Connected Networks of Excitatory and Inhibitory Spiking Neurons. J Comput Neurosci *8*, 183–208. 10.1023/A:1008925309027.

111. Izhikevich, E.M. (2006). Polychronization: computation with spikes. Neural Comput *18*, 245–282. 10.1162/089976606775093882.

112. Booker, S.A., and Vida, I. (2018). Morphological diversity and connectivity of hippocampal interneurons. Cell Tissue Res *373*, 619–641. 10.1007/s00441-018-2882-2.